Development of Advanced Model of Radar and Communication Signals Scattering on Wind Turbines

by

Kajengkhombi Chanu Wangkheimayum

to obtain the degree of

Master of Science in Electrical Engineering

at the Delft University of Technology,
to be defended publicly on Wednesday, November 1, 2017 at 13:00 hours.

Student number:	4513398	
Project duration:	March 13, 2017 – November 1, 2017	
Thesis Committee:	Prof. DSc. A. Yarovoy	TU Delft, EEMCS, MS3, Chair
	Dr. O. Krasnov,	TU Delft, EEMCS, MS3, Supervisor
	Dr. G. Janssen,	TU Delft, EEMCS, CAS
	Dr. F. Uysal,	TU Delft, EEMCS, MS3

The work was performed at Microwave Sensing, Signals and System Group, TU Delft

An electronic version of this thesis is available at `http://repository.tudelft.nl/`.

TU Delft

Acknowledgement

First and foremost, I would like to express my sincere gratitude to my thesis supervisor, Dr. Oleg Krasnov. With his constant guidance and support, I was able to successfully complete my thesis work. In spite of his busy schedule, he was always open for discussion and gave valuable feedback. His teaching approach makes every topic more intriguing and easy to understand. This was one of the many reason I chose to work under his supervision for my thesis.

I would like to thank Professor Dr. Alexander Yarovoy for giving me the opportunity to work in the Microwave Sensing, Signals and System (MS3) Group. During the span of these two years, I have followed most of the courses taught by him. His enthusiasm for teaching an encouragement to dig deeper into problems brings out the researcher in every student. His immense knowledge and expertise in the field of antennas and radar is laudable.

I would also like to thank the members of my thesis committee, Dr. Alexander Yarovoy, Dr. Oleg Krasnov, Dr. Ir. Gerard Janssen and Dr. Faruk Uysal for taking your time out in assessing my thesis.

This thesis journey was not an easy road, but it was made easy with the huge encouragement and support from my friends. Thank you Dhingra, Kotti, Qiaoqiao and Bhavuu for keeping me sane these past months, Ghina for the comfort food during ungodly hour, and my friends at BEST Delft. You guys made this journey feel easy.

To my friends, Pandey and Ritu, and my family back home, thank you for all the reassurance and guidance from literally 4900 miles away. Last but not the least, a big thank you to Pabung and Palem for always pushing me to strive for the best.

Abstract

In the recent years, there has been an increase in the popularity of renewable energy sources. One such being the wind energy. With the development in the field of wind energy, the structure of the wind turbines (WT) has also increased. The huge wind turbine structure (WTS) and the wind farms, both offshore and on-shore, has a strong impact on the radar signal communication. The wind turbine clutters (WTC), which is a result of strong Electromagnetic Interference (EMI), has affected the existing radar system such as air-traffic control, weather radars, *etc*. Thus, to mitigate the wind turbine clutters (WTC), there is a need to understand the scattering properties of the wind turbine structure (WTS).

The thesis proposes a development of a radar model to study the radar signal scattering on the wind turbine blades (WTB). The proposed model is developed in a simplified approach to study the time domain simulation of signal scattered on the WTS. The blades of the model are represented as linear wire structures, which are designed using thin wire approximation. It is implemented for arbitrary orientation of the WT with full 3-D polarimetry observation, which can be applied to different azimuth and aspect angle. The signal scattering from the WTB will be developed for mono-static scattering and bi-static scattering case. The scattering matrix was derived for the cases and the results of the different polarizations are analyzed.

The models developed until the date has been focused on high-frequency range (> 1GHz). To bring novelty to the model, it will be analyzed for very high (VH) and ultra high (UH)frequencies (50, 280, and 600 MHz). The Another feature of the model proposed includes the capability to simulate the range profile with arbitrary resolution. To implement this, pulse compression and stepped frequency waveform is used to attain high resolution with narrow-bandwidth. The results of the model will be validated using measurements data provided by the Agentschap Telecom, the Netherlands. The model is further extended to study the contribution of the mast in the signal scattering characteristics of the WTS.

Contents

List of Figures

List of Tables

1
Introduction

With the penchant for the renewable resources, there has been a rise in the development of these resources, wind energy is one such example. Recent years have seen a tremendous rise in the awareness and concern of the consumption of energy resources, as a result of climate change and global warming threats. These threats have led to a shift in the focus from traditional fossil fuels towards the development of renewable resources. One of the energy sources that is currently on the rise in demand is the wind energy. As an alternative source, wind energy presents itself as a viable source. To meet the expectations of the demands, there has been a rise in the development of the WTS. According to Wind Energy, previously known as EWEA, renewable energy accounted to 86 % for all the new power installations in EU and wind power covered 10.4 % of the EU's demand.

But what are the side effects of the rise of wind energy in the RADAR community?

In this chapter, the exploitation of wind energy's influence in the RADAR community will be discussed and the need to study this impact. The content of the chapter includes the problem definition, the research approach, and achievable goals. The chapter will conclude with a brief outline of the thesis report.

1.1. Problem Definition

The WTS has increased in huge number as result of the progression in the wind energy. This has lead to the surge in the wind farms, both onshore and offshore. In addition to their numbers, the is the size of the WT has grown. To accommodate better power production, the blades and the height of the WT have seen some significant improvement in size. As a result of this, the increase in the wind farms and WTS is having a great impact on the radar community. They result in what is known as the WTC due to the Electromagnetic Interference (EMI). These WTC interfere with the radar system such as as air-traffic control, and weather radar networks. It also gives rise to certain phenomena such as shadowing, scattering, and multi-path propagation. These results in less signal power for detection and causing a reduction in the range of operations. To reduce these WTC, the first step is to understand and study it's scattering properties and analyze them. Thus, the one of the primary motivation of the thesis is to understand the characteristics of the signal scattering from the WTS in low frequency bands.

The wind turbine generally consist of three WTB of dimensions around 50-60 m which are separated by a certain angle. The rotation or vibration of a part of the structure of the target induces micro-motion dynamics. The micro-Doppler effect is the Doppler modulation induced by these micro-motion. So, the rotational motion of the WTblades imposes a micro-Doppler effect on the signal scattered by it which are reflected back to the radar. As a result of the micro-Doppler, the carrier frequency encounters time-varying modulation due to the Doppler frequency shift. Recent techniques, included in most radar processing system to distinguish between reflections from a static and a non-static , are unable to differentiate between the Doppler effects imposed by these targets.The traditional FFT is not suitable to study the non-stationary micro-Doppler frequency features. Moreover, these micro-motions are sensitive to frequency bands of microwave frequency bands [7].

1.2. Research Approach

In this thesis project, the development of the simplified EM model is proposed to study the scattering properties of the WT blades and its influence on the reflected radar signal. The major scope of this project is to develop this model and analyze the results on the radar reflected signals accurately. To get a clear understanding of the research approach, the following questions are addressed.

How do we design this simplified model?
Firstly, the blades of the WT are modeled as a very thin finite linear wires using thin-wire approximation as proposed in [10][14]. The proposed model is broadening the scope of their work by extending to full polarimetry and including a 3-D model [14][10]. Despite the simplification, this model is expected to predict the behavior of radar returns in far-field region. This also allows the analytical derivation of basic closed-form solutions easily with less computational time and effort, which would otherwise take more effort. The model can be used for the interpretation of observation in time and Doppler domains. The incident wave is a plane wave since the radar is design to be located in a far distance from the WTS.

Since the model is designed as a 3-D model, it can be applied for different aspect angle by taking into account the full polarization of the scattered signals. The calculations and simulation will be done for various blades angles (azimuth/aspect angle θ and rotation angle ϕ), which depends on the rotation rate of the blade. To attain high-resolution of the target, the technique of multiple frequency and pulse compression is used in the model. It is addressed in detail in section 2.2.

Why is the contribution of the model in real time applications?
The clutter models developed till date are based some complex simulation techniques which either take long computational time or complex algorithm. But the proposed model helps in giving a result close to the real data without increasing the complexity of the model. To study the real time applications, the model is design for mono-static scattering and bi-static scattering cases. The studies of the scattering from the WTB are well documented for frequencies higher than 1 GHz. However, its study and observations are limited to lower frequencies. Various applications like GPS, air traffic control, $etc.$ uses the frequencies VH and UH frequencies bands.

To examine the micro-Doppler effect, the rotation motion of the blades can be analyzed by using range profiling of the radar response. It will give a graphical idea about the micro-motion. Lastly, the rotation of the WTB makes it difficult to mitigate it using existing ground clutter mitigation models. Micro-motions is the mechanical dynamics of a target in addition to its bulk motion. Thus, there is a need to scrutinized these micro-Doppler signatures to be able to mitigate them.

What are the ways to over the shortcoming of the traditional FFT technique?
The traditional signal analysis method is to apply a FFT to the signal in frequency or time domain. However, for non-stationary targets, the spectral contents vary over time and FFT cannot be used to represent the time-frequency properties. To overcome the deficiencies of the traditional Fourier transform, the most simple and direct approach is to use short-time Fourier transform (STFT) (section 2.4).

Why is the model expected to work better at VH and UH frequency bands (50, 280, and 600 MHz)?
The blades of a WT usually has a conducting wire of radius of a few mm to protect the structure from lightning. For thin wire approximation, it is assumed that the radius of the wire structures are very small compared to the length of the wire. Working in these frequency bands gives us wavelength of 1 m to 10 m, which is comparable to the length of the WT blades and mast. With the increase in the frequency, the wavelength will decrease, and the assumption of thin linear wire structure will cease to be valid.

How will be the results of the model authenticated?
The proposed model is entirely theoretical and is based on mathematical derivations. In order to authenticate the results of the model, it need to be validated. To do this, the results of the proposed model are verified using real-time measurements provided by the Agentscahp Telecom, the Netherlands.

Thus, the main objective of the thesis project to be cultivated at the end of this project is
The development of a simplified electromagnetic model to study the signal scattering of WT blades and mast

at low frequencies (VH and UH frequency bands) for polarimetry RADAR.

1.3. Novelty

In theory, the main novelty of the thesis project is the full polarimetry extension of the model at VH and UH frequency bands. It is implemented using stepped frequency pulse compression approach with range profiling of the WT radar response. On the other hand, the reflected radar signals from the WT which constitute a time varying Doppler component are more sparsely represented using STFT.

The novelty of the thesis project is summarized as follows

1. Full Polarimetry Extension of the model proposed in [10, 14]
2. Range profiling of WT signal using stepped frequency pulse compression.
3. Model application and validation for the VH and UH frequency bands
4. Study of influence of mast in the wind turbine scattering.

1.4. Outline of the Thesis

The following chapters (2- 7) will give an insight into how the research objectives defined were throughly followed. The chapters are structured as follows

Chapter 2 highlights the background information related to this thesis *viz.* radar polarimetry, micro-Doppler, radar profiling, etc. to understand the research approach clearly.

Chapter 3 highlights the different techniques and methodologies addressed in various studies present in the literature. It also discusses about the state of art of the wind turbine scattering models.

The detailed design of the mono-scattering and bi-scattering model is discussed in details in chapter 4.It includes derivations of the scattering matrix for both the case. The bi-scattering matrix of the mast is also presented in brief in the section.

Chapter 5 describes the measurement set-up of the real-time data obtained from the Agentschap Telecom. The measurement set up and the techniques used in carrying out the experiment is discussed in this chapter.

Chapter 6 involves the results and analysis of the data obtained from the theoretical analysis of the model for mono-scattering, bi-static scattering, and the influence of the mast in the WT scattering. It discuss the results obtained from the proposed model with different factors such as window function, different polarization, range profiling, etc.

Chapter 7 concludes the thesis with the discussion of the results attained and the recommendations for future research.

2

Theoretical Background

To understand the development of the proposed model, it is necessary to understand the underlying concepts and design basics. This chapter helps in understanding the basics by providing some background information. The topics covered in this chapter will give clear understanding to the model design and the chapters following.

2.1. The Radar Range Equation

The radar range equations is a simple formula which can be used to calculate the received power of the waves reflected from a target of interest. The radar equation for a mono-static radar can be represented using the following equation.

$$P_r = \frac{P_t G^2 \lambda^2 \sigma}{(4\pi)^3 R^4} \tag{2.1}$$

and for the bi-static radar, it is given as

$$P_r = \frac{P_t G_t G_r \lambda^2 \sigma_{bi-static}}{(4\pi)^3 R_t^2 R_r^2} \tag{2.2}$$

where
P_t = Peak transmitted power in watts (W)
P_r = Received power
σ = Radar cross section (RCS) in square meters (m^2)
λ = Wavelength in meters m
G_t = Gain of the transmit antenna
G_r = Gain of the receive antenna
R = Range between the mono-static radar and target in meters
R_t = Range between the transmitter and target
R_r = Range between the receiver and target

Radar Range Resolution

The radar range resolution, typically denoted by ΔR, determines how well the targets can be distinguished from each other and can be detected by the radar. If the targets are spaced less than ΔR, the radar will fail to detect the target. The range of the target R is determined by measuring the time delay ΔT, which is the time taken for the signal to travel to the target and returned to the radar. 2.3 and 2.4 gives the expression for range resolution and range respectively, where τ is the pulse width, B is the signal bandwidth, and c is the speed of light.

$$\Delta R = \frac{c\tau}{2} \tag{2.3}$$

$$R = \frac{c\Delta T}{2} \tag{2.4}$$

To avoid range ambiguities, the Pulse Repetition Interval (PRF) should be long enough (or the Pulse Repetition Frequency (PRF) should be short enough) such that the reflected signal reaches the radar during this time interval (or before the transmission of the next pulse) [15]. The following condition must be applied to avoid the range ambiguities

$$PRI \geq \Delta T_{\max} = \frac{2R_{\max}}{c} \quad or \quad R_{\max} \leq \frac{c.PRI}{2} = \frac{c}{2PRF} \tag{2.5}$$

The maximum range that can be measured by the radar distinctly without any ambiguity is called the unambiguous range, R_{ua}. It is given by

$$R_{ua} = \frac{c}{2PRF} \tag{2.6}$$

Radar Cross Section

RCS is defined as the scattering or reflective property of an object. It represents the strength of the echo of the signal reflected by the object to the radar. It is the ratio of the power reflected per solid angle unit to the incident power density per 4π given by

$$\sigma = \lim_{R\to\infty} 4\pi R^2 \left|\frac{\mathbf{E^s}}{\mathbf{E^i}}\right|^2 \tag{2.7}$$

where $\mathbf{E^s}$ and $\mathbf{E^s}$ represent the scattered field and the incident field. Without near-field effects, *i.e.*

$$\sigma = \lim_{R\to\infty} 4\pi R^2 \frac{P^s}{P^i} \tag{2.8}$$

where P^s and P^i is the scattered power and incident power density. The RCS can be characterized as mono-static when the transmitter and receiver are co-located, or bi-static when the transmitter and receiver are placed in different locations. The RCS has units of square meters (sqm) m^2

Range Profile

A radar range profile can be viewed as an 1-D 'image' of an object, where a part of the object reflects the radar signal (radar return). The radar returns are projected onto the line of sight (LOS) for some particular aspect angle [16][17]. This is exemplified in Fig. 2.1. It also represents signatures of some target structures, such as the size of the target, scatterer distribution [18]. To achieve high-resolution range profile, it requires a wide-bandwidth system. The technique to achieve high-resolution range profile is discussed in the next section.

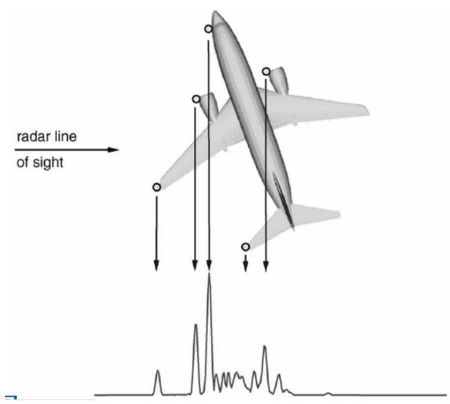

Figure 2.1: Randar range profile of an aircraft [1]

2.2. Pulse Compression

The range resolution (2.3) of a radar depends on the pulse width. For a good detection range, the strength of the received signal needs to be strong. The pulse should have more energy content to be able to propagate without attenuation for long distance during the transmission. To attain maximum peak power, short pulses are required, and the short pulses result in low range resolution. Thus, the range resolution cannot be increased without compromising the peak power which is limited by the transmitter. To attain better range detection with long pulses and fine range resolution with short pulses, the technique of *pulse compression* is used. This method improves the range resolution without affecting the peak power for transmission. The range resolution is given by

$$\Delta R = \frac{c}{2B}$$

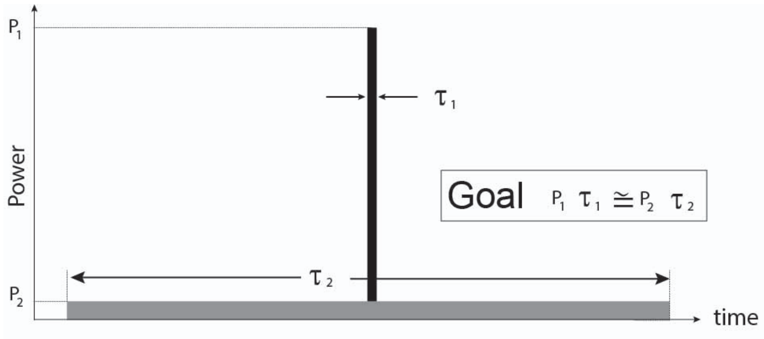

Figure 2.2: The pulses illustrated have same energy content with different pulse length and power [2].

Pulse compression can ensure fine range resolution, but the high bandwidth of the signal can prove to be difficult for signal processing. To improve this problem, the pulses are transmitted with different carrier frequencies which are modulated linearly. The high-resolution range profiles are achieved from these sequence of pulses, eliminating the need for a wide instantaneous bandwidth. Hence, the stepped frequency method results in a overall wide bandwidth overall but a narrow instant bandwidth [19].

The frequencies in this technique are spread over the bandwidth B for a constant frequency step size Δf from pulse to pulse, given by 2.9, where the frequency of each pulse is incremented by Δf from the preceding pulse. At every stepped frequency, the phase and amplitude of the reflected signal are sampled, assuming that the target moves with a constant velocity.

$$\Delta f = f_{n+1} - f_n = \frac{B}{N-1} \tag{2.9}$$

$$f_n = f_o + n\Delta f \tag{2.10}$$

where
f_n = Carrier frequency at which the n^{th} pulse is transmitted.
f_o = Central frequency.
B = Bandwidth of the signal.
N = Number of pulses.

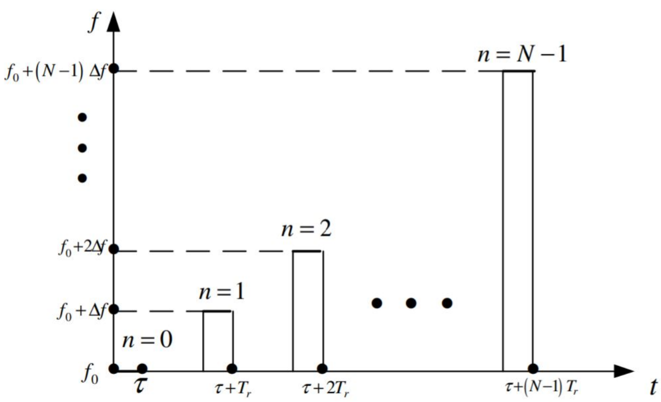

Figure 2.3: Illustration of stepped frequency waveform [3].

The total bandwidth of the system using stepped frequency becomes $(N-1)\Delta f$ and the range resolution is

$$\frac{c}{2(N-1)\Delta f}$$

.

2.3. Doppler Effect in Radar

When an Electromagnetic (EM) signal is transmitted by a radar to a target, the signal interacts with the target and is reflected to the radar. For an object which is in motion, the frequency of the reflected signal will have a Doppler frequency shift. This shift depends on the radial velocity of the object and the wavelength of the signal transmitted [20]. The round-trip Doppler shift (f_D) is given by

$$f_D = -f\frac{2v}{c} \tag{2.11}$$

where c is the speed of light , f is the frequency transmitted by the radar and v is the velocity of the object in motion along the radar line of sight (RLOS).

If the object or the target has micro-motions, like vibrations or rotations, the radar return will be different from the object with a radial velocity. The micro-motions of the object might induce a periodic frequency modulation on the reflected signal, as a result, it will generate sideband around the Doppler frequency of the target. This phenomenon is called the micro-Doppler effect [4].

Often targets like helicopters and wind turbines incorporate vibrating or rotating structures because of their mechanical design. The micro-Doppler shift can be induced by vibration, rotation, tumbling or precession (coining, spinning, and nutation) of the object. However, the point of interest of the present study lies in the rotation of the object, since one of the primary reasons for the micro-Doppler shift in the WTs is the rotation of blades.

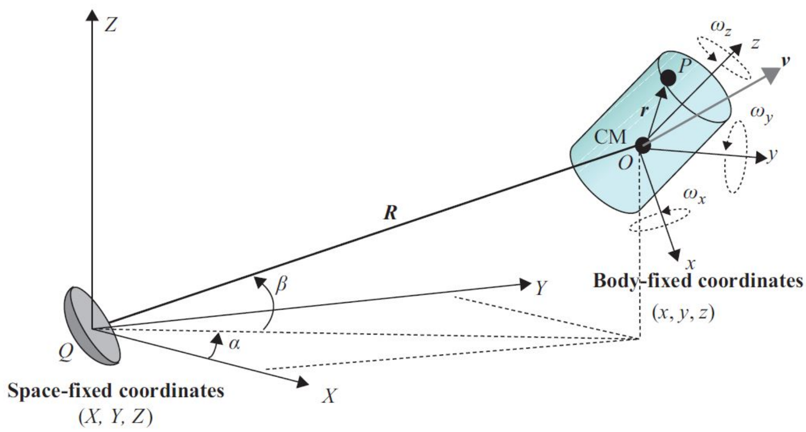

Figure 2.4: The coordinates (space-fixed and body-fixed) to illustrate the target motion [4].

For simplicity, it is assumed that the object of interest is a rigid body. A rigid body is a solid body in which deformation is zero or so small it can be neglected. The motion of a rigid body can be understood using Fig. 2.4. The origin of the body-fixed system is the center of mass of the body. The space-fixed system is also at the origin of its coordinates. Then, the range vector **R** represents the distance between the origins of the two systems.

If **Ω** is the vector representing the angular velocity of the rotation of the body, then the position of an arbitrary particle, P, in the body-fixed system will be given by **R+r** and its velocity will be given by

$$\frac{d}{dt}(\mathbf{R}+\mathbf{r}) = \mathbf{v} + \mathbf{r}\,\boldsymbol{\Omega} \tag{2.12}$$

where v is the translation velocity of the center of mass of the rigid body, **r** is the distance from the origin to the point P, and $\mathbf{\Omega} = (\omega_x, \omega_y, \omega_z)^T$ is the angular velocity vector with angular rotation velocities about the axes of the body-fixed system.

2.3.1. Rotation Induced Micro-Doppler Shift

The body-fixed diagram in Fig. 2.4 is taken as a reference coordinate system (X', Y', Z') and the geometry of the rotating object where α and β denote the azimuth and elevation angles of the object in the reference coordinate system $(X', Y'Z')$.

If the object is rotating, any point on it will move to a new position in the reference coordinate system (X', Y', Z'). This new position can be calculated using initial position with a rotation matrix.

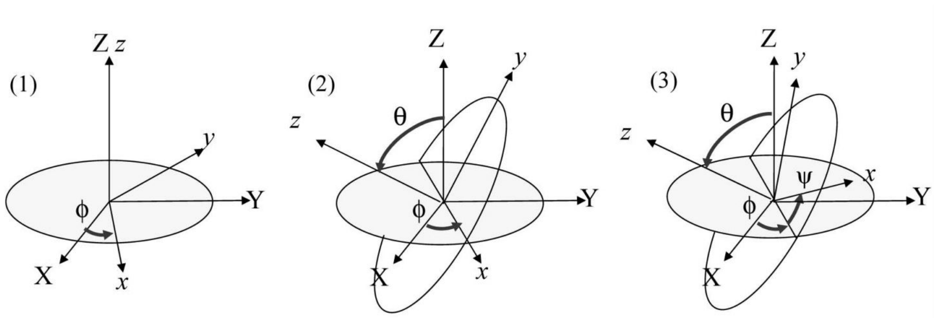

Figure 2.5: Rotation of the Euler angles (ϕ, θ, ψ) [4].

To exploit the time-varying micro-Doppler characteristics, a high-resolution and time-frequency analysis method must be used. This explained in detail in the following section.

2.4. Short-Time Fourier Transform (STFT)

With the rotation of wind turbine blades (WTB), the frequency of the reflected signal will change over time, which is known as the Doppler frequency shift. The traditional signal analysis method is to apply a Fourier transform to the signal in frequency or time domain. However, for non-stationary targets, the spectral contents vary over time, and Fourier transform cannot be used to represent the time-frequency properties. To overcome the deficiencies of the traditional Fourier transform, the most direct and straightforward approach is to use STFT.

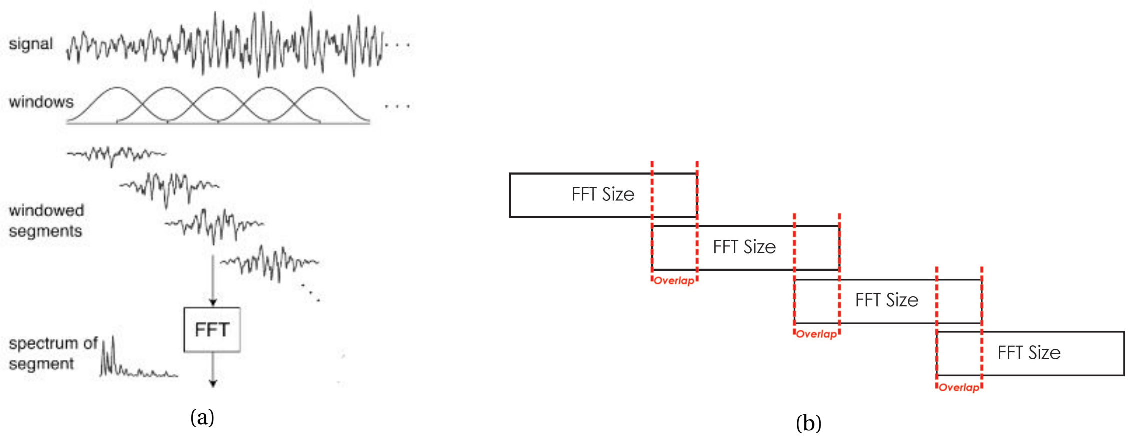

Figure 2.6: Process explaining the working of STFT. (a) The window functions are applied to the segments with a defined amount of overlap; (b) The FFT is applied to the segments separately [2].

An STFT is obtained by dividing the signal into time intervals and applying the Fourier transform to each of these segments separately, assuming that the signal is stationary during this time interval. But the Fourier transform will cause an abrupt discontinuity in the signal. To avoid this, a set of overlapping window function is applied to the segments that zeros all but a short time interval [21]. The amount of overlap determines the time-frequency resolution of the signal. The STFT is a discrete-time Fourier transform (DTFT) for fixed time analysis. The mathematical representation of STFT of a signal $s(t)$ is given as

$$STFT_s(t,\omega) = \int_{-\infty}^{+\infty} s(\tau)h(\tau - t)e^{-i\omega\tau}\,d\tau \tag{2.13}$$

where $h(t)$ is the window function, t is the time parameter, and ω is the frequency parameter.

To represent the STFT graphically, a spectrogram is used. The spectrogram is calculated by using STFT and is represented by the squared magnitude of the STFT without keeping phase information of the signal. From the micro-Doppler signature represented in the spectrogram, the rate of rotation, the length of the blade, the number of blades, and also the speed of the tip can be estimated.

$$\text{spectrogram}(t, f) = |\text{STFT}(t, f)|^2 \tag{2.14}$$

Fig. 2.7 shows the resulting spectrogram for different time overlaps. The image is very pixelated for lesser overlap. With a larger amount of overlays, the transition gets smoother and continuous as the discontinuity from the FFT decreases after the windowing. The axes of the spectrogram represent frequency and time. It contains information on the frequency content of the signal at different time instances [4].

As the length of the window decreases, the time resolution improves while the frequency resolution deteriorates. It is common to make a compromise between time resolution and frequency resolution to select the length of the window function.

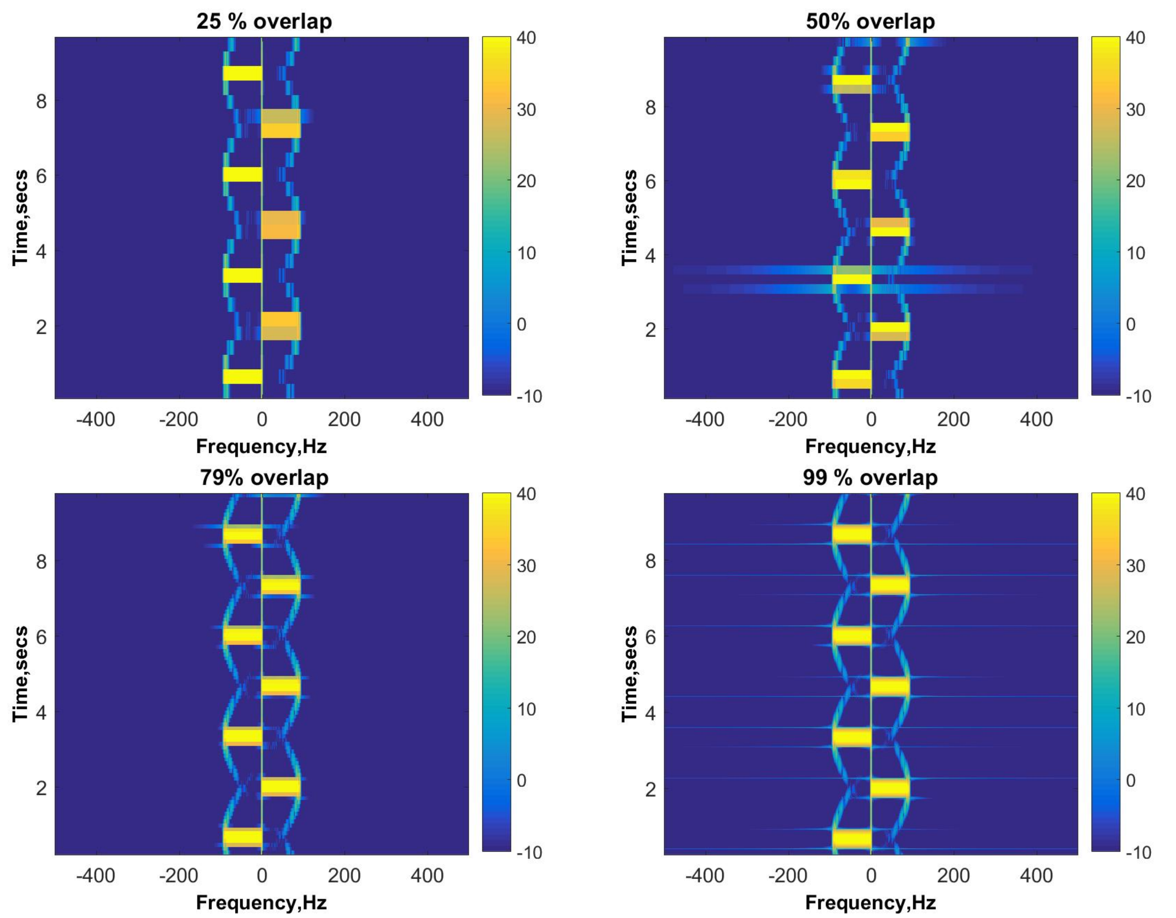

Figure 2.7: Spectrogram is illustrating the effect of different time overlaps.

2.5. Electromagnetic Interference and Scattering

WTs causes electromagnetic interference (EMI) as a result of the following mechanisms:

1. Near-Field Effects
   In general, the near-field effect is the potential of the nearby objects or surrounding to interfere the radio signals due to the EM fields emitted. In case of a WT, the generator, the nacelle (It is a cover housing that includes all the generating components of a wind turbine) or hub has the potential to introduce near-field effects on the WTBs scattering [22].

2. Diffraction
   When a wavefront's path of travel is disrupted by an object, the path is deviated or modified from the initial path. This is called diffraction. It can also occur when the object absorbs the signal [22].

3. Reflection (or Scattering)
   This occurs when the WT either reflects or obstructs the transmitting signals. The large dimensions of the WT blades and the height of the mast increases the susceptibility of the signal to scattering. In this situation, the received signals are out of phase (time delay) or distorted compared to the transmitted signal.

In this thesis, the main focus is on the signal scattering from the WTs. The total field at an observation point due to radiation by incident fields on the WT blades will be comprised of the scattered signals. If the scattered field is directed back towards the source, it is known as mono-static scattering. If the directed field is directed in a different direction and not towards the source of the signal, it is called bi-static scattering.

2.6. Polarization and Scattering Matrix

Radar polarimetry deals with polarized EM waves. By definition, it is the science of acquiring, processing and analyzing the polarization state of an EM field. Non-polarimetry radar deals with only a single type of polarization, for both transmission and reception. However, this limits the application of these radar as it measures the signal in only one-dimension. Thus, a polarimetry radar is more applicable in studying real-time applications.

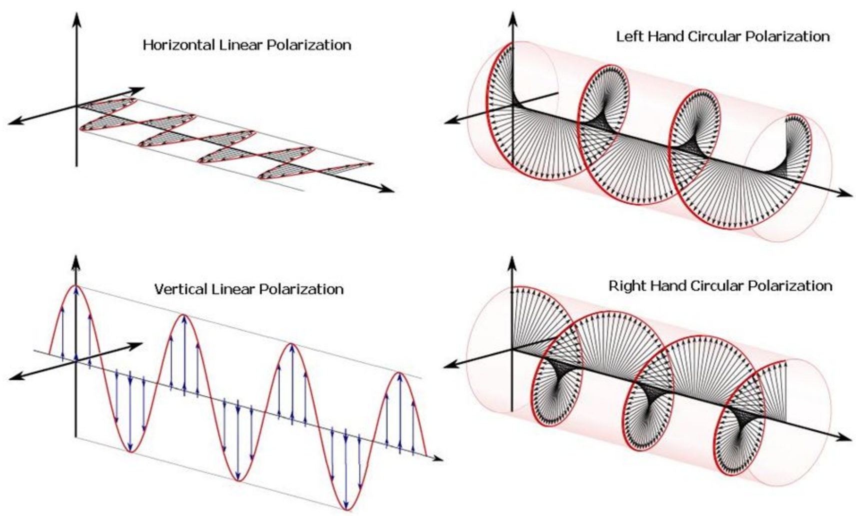

Figure 2.8: Illustration of the different kinds polarization.

The polarization of an EM wave describes the motion and orientation of the electric field vector [15]. Polarization can be defined as the changes in the direction of field vector as it travels. The polarization of an EM wave is influenced by the shape and size of the object from which it reflects and is different for every object. Therefore, the polarization of an EM wave also helps in determining the geometry of the object.

There are three types of polarization, *viz.*, linear, circular, and elliptic illustrated in Fig. 2.8. However, for the present thesis, only linear polarization is important. 2.15 represents the electric field of a linearly polarized plane wave.

$$E(t) = E_0 \cos(\omega t - kz) e_x + E_0 \cos(\omega t - kz) e_y \tag{2.15}$$

An EM wave is linearly polarized if one component is zero and the electric field oscillates along the axis of the non-zero component. For instance, if the y-component is zero and x-component be the non-zero component, then the EM wave is said to be linearly polarized in the x-direction. If x represents a horizontally oriented axis, the wave is horizontally polarized. In general, the polarization is linear if the x and $y$components differ in phase by an integer multiple of π radians; the relative phase between the x-component and y-component is $\mathbf{n}\pi$. The angle of the polarization depends on the relative magnitudes of E_x and E_y [15].

Horizontal polarization ($E_h/E_{||}$) is the state where the electric vector is orthogonal to the plane of incidence. Vertical polarization ($E_v/E_\perp$) is the state where the electric vector is parallel to the incident plane.

A polarimetry radar utilizes two polarization schemes resulting in four channels for the transmission and reception. They are:

1. **HH**: Horizontal transmission, Horizontal reception.
2. **HV**: Horizontal transmission, Vertical reception.
3. **VH**: Vertical transmission, Horizontal reception.
4. **VV**: Vertical transmission,Vertical reception.

The scattering matrix, S, for the given frequency and orientations of radar and target, contains all the information concerning the scattering properties of the target. The backscattering properties of the target can be completely described by the scattering matrix. An arbitrary plane wave which is polarized can be expressed as a sum of two orthogonal plane waves of general polarization. The transmitted and received field can be shown as

$$\begin{aligned} E_1^S &= S_{11} E_1^S + S_{12} E_2^T \\ E_2^S &= S_{21} E_1^S + S_{22} E_2^T \end{aligned} \tag{2.16}$$

where E_T and E_S represent the transmitted field and scattered field.

$$\begin{bmatrix} E_1^S \\ E_2^S \end{bmatrix} = \begin{bmatrix} S_{HH} & S_{HV} \\ S_{VH} & S_{VV} \end{bmatrix} \begin{bmatrix} E_1^T \\ E_2^T \end{bmatrix} \tag{2.17}$$

$$\mathbf{S} = \begin{bmatrix} S_{HH} & S_{HV} \\ S_{VH} & S_{HH} \end{bmatrix} \tag{2.18}$$

The coefficients of the matrix in 2.17 denoted by **S** is called the *polarization scattering matrix* which describes the transformation of the E-field of the incident wave to the E-field of the scattered wave. The diagonal elements, S_{HH} and S_{VV}, of the scattering matrix are known as *co-polar* terms and the off-diagonal terms, S_{HH} and S_{VV} are called *cross-polar* terms as they relate the vertical and horizontal polarization state. For backscattering, the reciprocity theorem mandates that $S_{HV} = S_{VH}$ [23]. The transmitted and the scattered field can be also expressed as

$$\mathbf{E_S} = \frac{e^{-jkr}}{r} S\mathbf{E_T} \tag{2.19}$$

The term $\frac{e^{-jkr}}{r}$ takes into account the propagation effect in amplitude and phase, where r is the distance from the center of the target to the point of observation and k is the wave number [23].

2.7. Conclusion

This chapter gave information regarding the radar polarimetry, range profile etc. which helps us in understanding the basic concepts used in this thesis. The micro-Doppler provides significant information about the targets. The limitations of FFT was solved using the STFT. The pulse compression technique was also highlighted in the chapter. It is important to understand this to get a proper analysis of the defined problem. In the following chapters, the application of these concepts will become more evident.

3
Literature Review

Numerous work has been done to study the influence of WTs through different techniques. This has been achieved by implementing a scaled model, by using computational methods like finite element method (FEM), method of moment (MoM) or finite-difference time-domain (FDTD), or using approximation methods including approximation based on geometrical optics (GO) method and approximation based on the current such physical optics (PO). This chapter discusses the results of different methods which are used to analyze the EM scattering characteristics of the WT and the basis of the development of the present model.

3.1. Wind Turbine and Radar

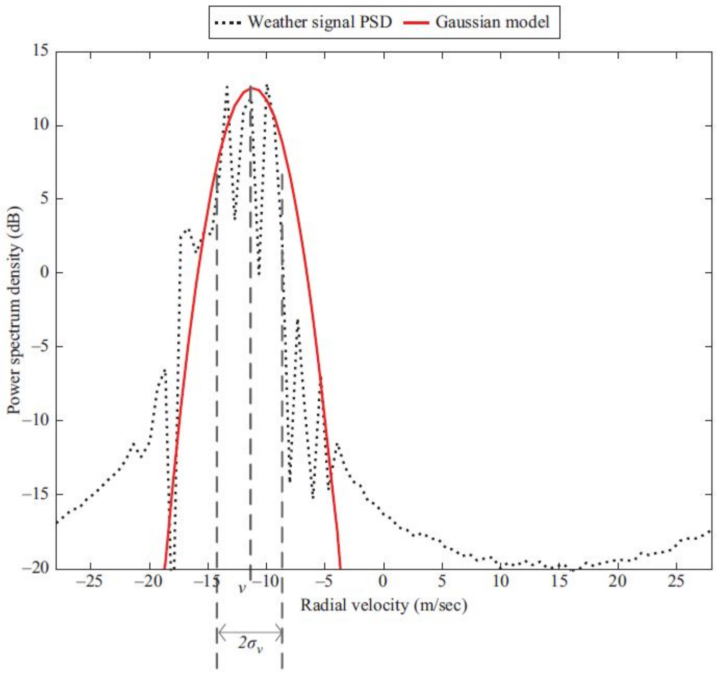

Figure 3.1: PSD comparison of ground clutter and rotation of the blades [5].

The WTs, due to their large size and continuous movement of their parts, may cause interference in the signal propagation and radar detection. With the increase in demand to harvest its potential, there is a rapid increase in the number of wind farms, which is alarming for the radar community. Closely spaced WTs may cause diffraction resulting in shadowing effect around the wind farms. Regardless of the spacing between the WT, the size of the structures can still impact nearby performance, acting as clutters. But this clutter, called WTC is different from the traditional ground clutters. The ground clutters are stationary from pulse to pulse.

However, the WTCs have complicated micro-Doppler features, addressed in section 2.3, due to it blades' rotation.

To understand the differences between the ground clutter and WTC, Fig 3.1 shows the comparison of the PSD. The Gaussian Model Adaptive Processing (GMAP) technique has been applied in the WSR-88D system [24]. But GMAP can suppress only the stationary parts of the wind turbine and seems to have no impact on the WTC as the clutter from the micro-motion is spread out for the entire Doppler spectrum.Hence, there is a need to figure out a way to mitigate the WTC since the conventional techniques to reduce ground clutters would fail to work. To mitigate the WTC, the characteristics of the signal scattering from the WTS need to be studied before to the development of mitigation techniques.

From [25], it is learned that the large windmills can have EMI on TV signals at very high frequency (VHF) and ultra high frequency (UHF) bands. Various work has been carried out to study the signal scattering from the WT [26][4][27]. These studies provide a basis for the development of models for estimating the scattering pattern of WT and determine their potential impact on television reception quality [28][29][30]. There are several scattering models developed to check on this issue. The comparative analysis of the different methodologies such as PO, geometric theory of edge diffraction (GTD),etc. has been analyzed in [31].

3.2. Theoretical Models for Wind Turbine Scattering Estimation

The modeling of the radar cross section (RCS) and Doppler signatures of various models of WTs is vital in the prediction of the effect of the WTS [32]. Variety of research has been carried out to develop the models of RCS acurateand to measure the influence of different azimuthal orientation and rotation speeds on the resulting radar return of the scaled models for WTs .

3.2.1. Scaled Model

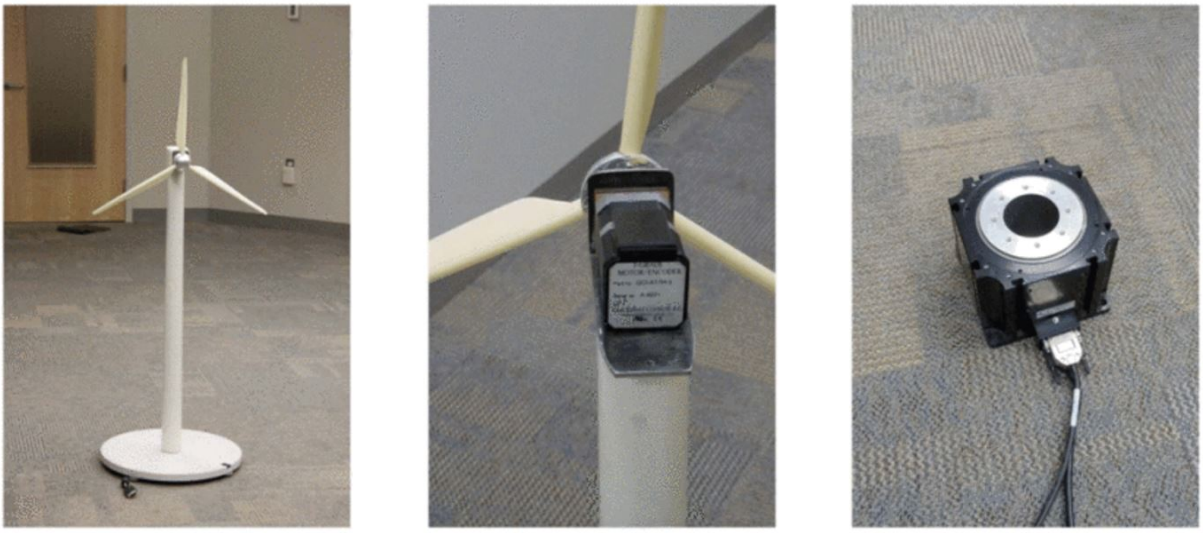

Figure 3.2: The scaled WTM is placed in an anechoic chamber showing the rotor inside the opened nacelle, and the base rotor used to rotate the blades. The scaled model is customized to mimic a real wind turbine [4][6].

The big size of the wind turbine makes it infeasible to study the physical parameters and the spectrum characteristics. The solution to this predicament is to scale-down the model and examine the micro-Doppler signatures and radar returns in a controlled environment.

A scaled WTM is shown in Fig 3.2 [6][33]. The model was built with a tower height of $1.2m$ and a rotor diameter of $0.7m$. The fact that the scaled model can retain the geometry of the actual WT acts as an advantage of the scaled model. The frequency domain measurements were carried out using a VNA. The simulation was done using the X-band Laboratory radar (LR).Fig 3.3 plots the average power of the radar return for the different blades position. The reflections from the surroundings of the scaled model can be observed in the figure. The smaller peaks with lesser power are a result of the impedance mismatch at the cables, antennas, etc.

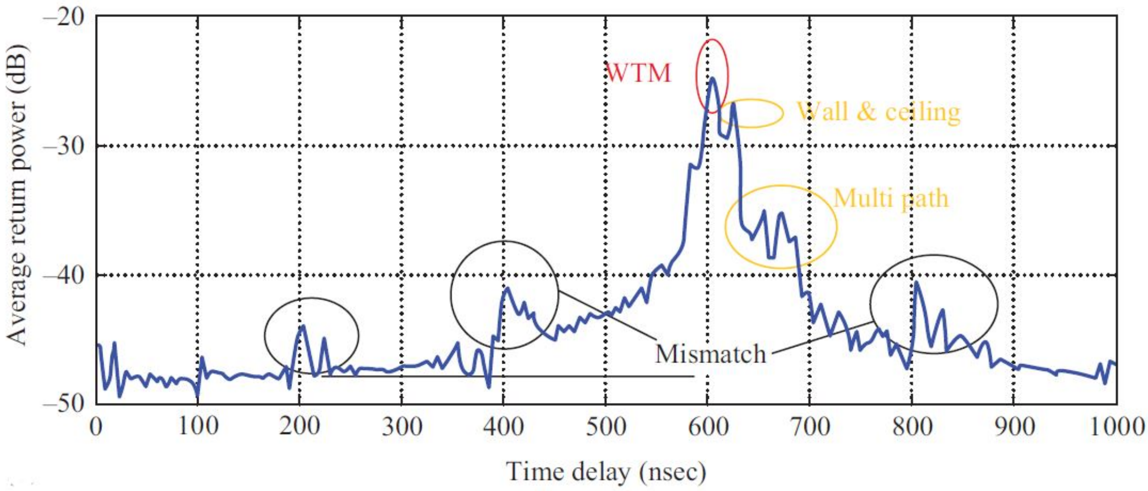

Figure 3.3: The average power of the radar return which is illustrating the additional peak as a consequence of multi-path due to the nearby objects [7].

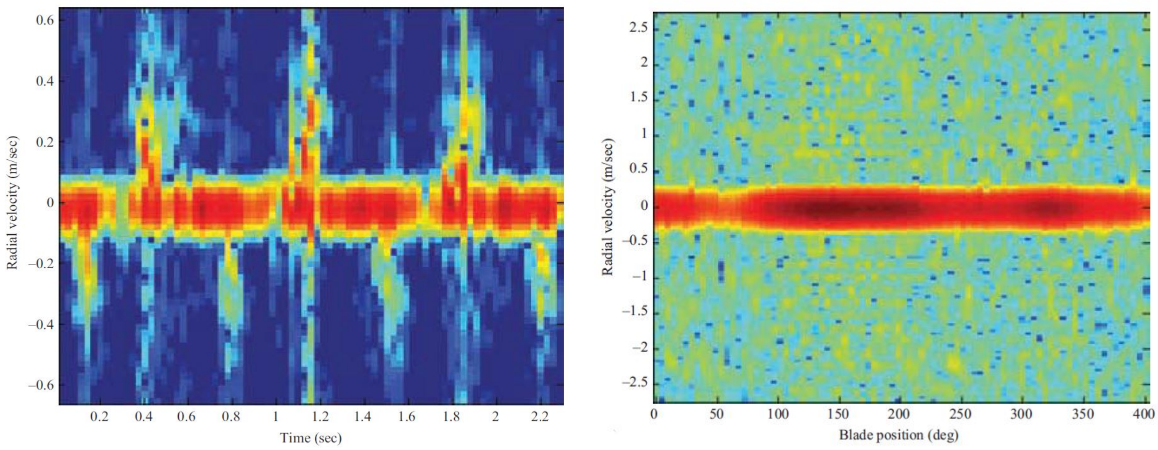

(a) (b)

Figure 3.4: Spectrograms of time domain measurement for different aspect angles: (a) Aspect angle $\theta = 90°$; (b) Aspect angle $\theta = 0°$ [7].

The spectrogram of the scaled model is shown in the Fig. 3.4 for the aspect angles of $\theta = 0°$ and $\theta = 90°$. The flashes observed in the figure, the six peaks, occur when the blades are perpendicular to the RLOS, *i.e.*, ϕ becomes a multiple of $\pi/3$. The trajectory sinusoidal variation of the blade tip is not visible due to low resolution. This can be seen prominently in cases when the Doppler resolution is better. These cases will be addressed in section 3.4. In Fig. 3.4b, the radar return is constant with a maximum value. This is because the radar returns remain constant throughout the rotation of the blade for the specified aspect angle, equivalent to the radar returns from a stationary clutter. Theoretically, it should remain constant without any variation, but it is not due to the near-field effects. In this case, the wind turbine clutter can be mitigated by conventional ground clutter filtering.

The two side of each spectrogram in the Fig.3.5 are very different. The radar return is negative when the blade is coming towards the radar, and the flash for this case is because of the downward sweep of the blades.

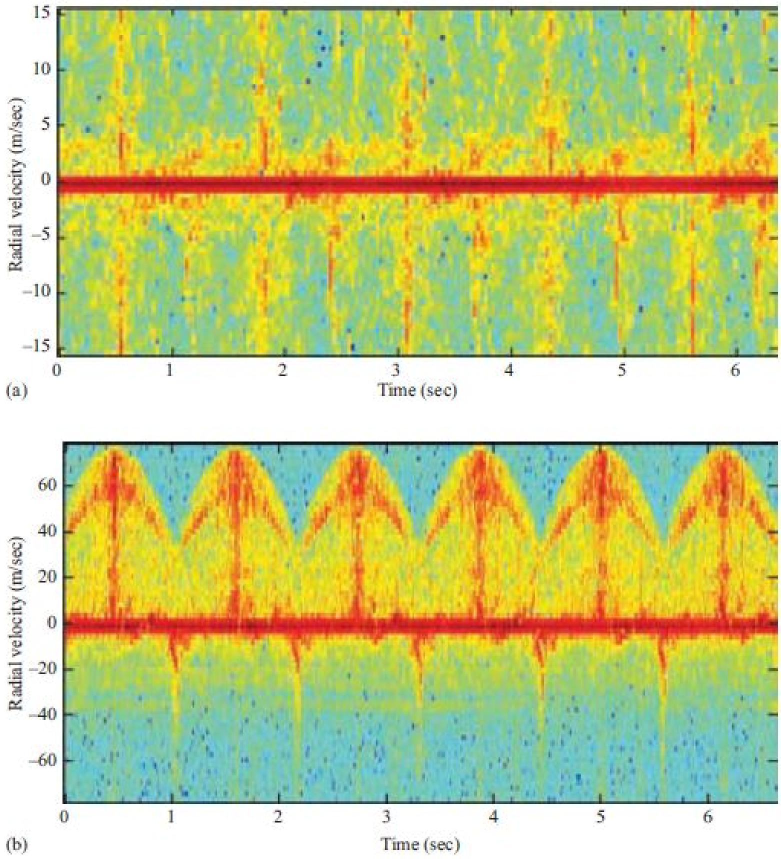

Figure 3.5: Spectrogram of the field measurement of the wind turbine (GE 1.6MW) respectively for aspect angle of $\theta = 270°$: (a) PRF = 2 kHz; (b) PRF = 10kHz [7].

The mean has three major peaks at $\theta = 90°, 180°, 270°$, which corresponds to the three aspect positions shown in Fig.3.6. As the WTBs moves to 90° or 270°, one side of the nacelle which is perpendicular to the RLOS results in a peculiar observation. The rear side of the nacelle causes a peak at $\theta = 180°$. The standard deviation is also highest at $\theta = 180°$ which can be attributed to the reflection from the backside of the blades. Therefore, to reduce the interference in the radar signal, normal incidence should be eliminated by proper nacelle design [7].

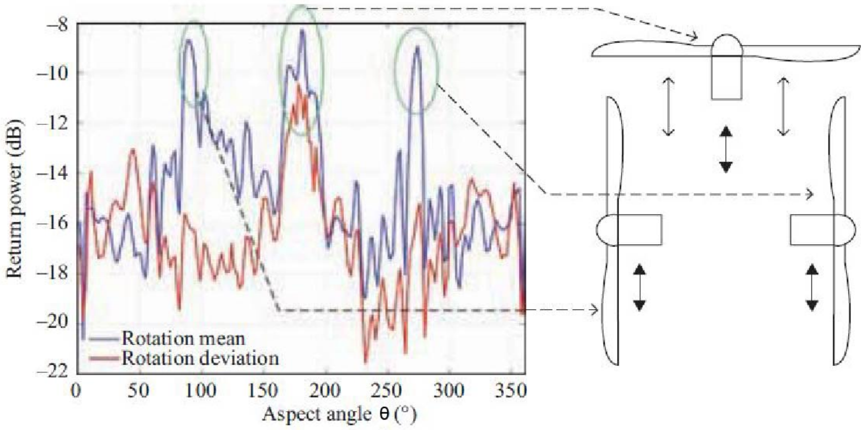

Figure 3.6: Mean and standard deviation of return power in terms of the aspect angle [7].

3.2.2. In the presence of ground

In addition to the existing problem of WTC, there arises another issue with the multi-path effect of the return signal from the ground bounce [34]. In the study reported in [5], the influence has been studied using a point scatter model and image theory to compute the backscattering from WT above ground. Another approach was made using a high-frequency ray tracing code, Ahilo. The results of the point scatter model were verified using the results from Ahilo. The simulations were done for a radar frequency of 1 GHz with the blade length of 30 m, and a turbine height of 60 m above an infinite ground place. The observations are done with a radar located at an angle of elevation 20° and 90° yaw angle from the turbine.

The following figures show the backscattering result from the two cases. For the point scatter model, the Doppler features arise as a result of blade flashes. The halo-like result around the tip is due to the scattering from the tip of the blades. In Fig. 3.7b and 3.7c, additional flashes were observed. The single-ground bounce mechanism also produces a specular reflection from the tower which is the reason for the stronger DC frequency component in Fig. 3.7d. Fig. 3.8 illustrates the resulting extra flashes (i) and (ii) using image theory. It can be noted that the maximum Doppler of (i) is less than that of (ii) because the radial velocity of the blade relative to the source and observer is lesser than the other cases.

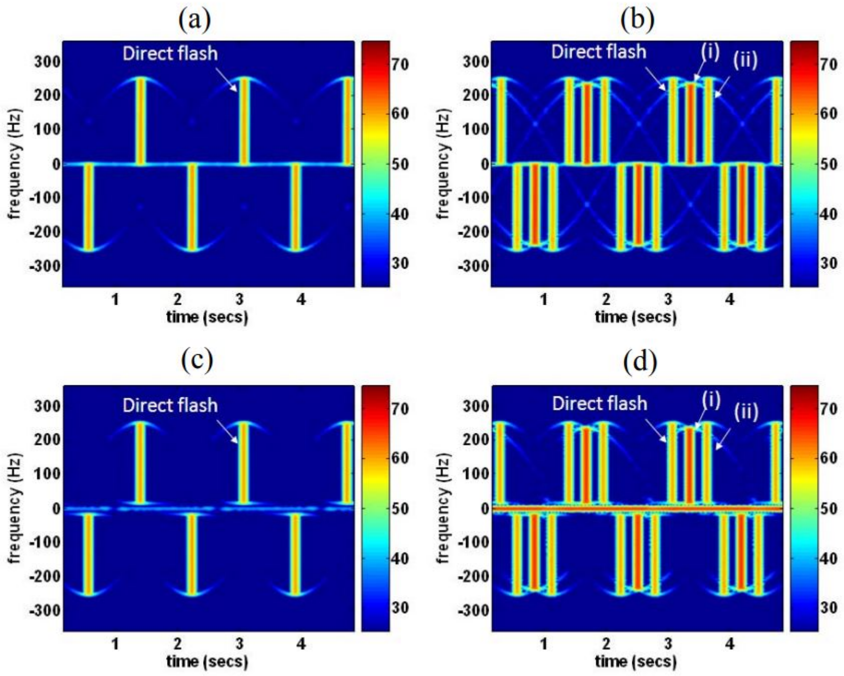

Figure 3.7: Spectrograms for backscattering (a) Without point scatter model. (b) In the presence of ground using point scatter model. (c) Without ground using Ahilo. (d) In the presence of ground using Ahilo [5].

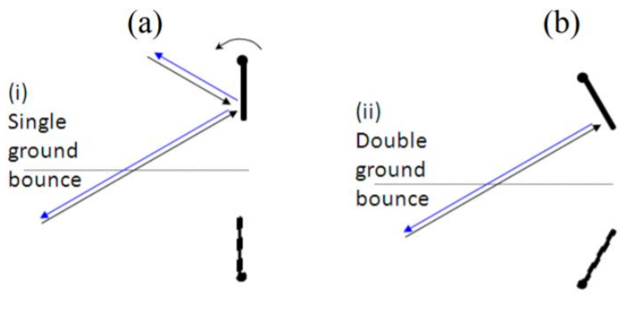

Figure 3.8: Image theory explaining the new flashes in the results of the point scatterer model and Ahilo.

However, another extensive study of the radar scattering from WT in the HF frequency bands has been done [35]. The WT is modeled as thin wires [8]. The ground plane is assumed as a perfectly conducting infinite ground plane to model the water surface. This is because the HF frequency range is associated with ocean currents.

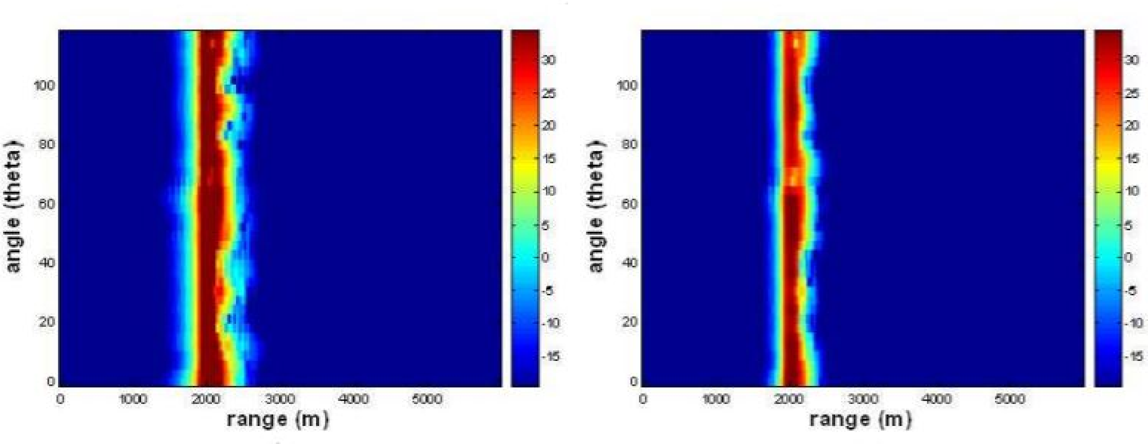

Figure 3.9: Effect of the conducting ground surface on the turbine RCS(a)RCS versus range and blade angle in the presence of ground (b)RCS versus range and blade angle without ground.[8].

3.3. Mast Contribution

A WT is composed of a tower, a nacelle, and a rotor with usually three blades made of non-metallic material [36]. The area of interest in studying the signal reflected is on the motion of the blades due to its broad mechanical structure and the micro-motion [37]. The signal reflected back from the nacelle, or the tower (mast) is overlooked. It can be seen in most of the analytical models or software tools that study the impact of WT, mainly focuses on the blades of the WT. The contribution of the mast of the WT is seldom taken into account, but it might have a significant impact on the clutter study or model designs and thus, should not be overlooked. The study on this issue has been carried out in [9] using the method of PO [38][39][40][41].PO provides an analytic tool for the calculation of the RCS for a variety of targets and circumstances and is a high-frequency approximation method that provides accurate results for electrically large objects ($L \geq 10\lambda$). It is based on the estimation of the field strength values radiated by the induced currents on the illuminated portions of a target surface [9].

The PO facets program, developed in MATLAB, utilizes the PO method to compute the surface currents on the triangular facets that comprise the building blocks of a target model.The model is designed in CAD as a composition of multiple triangles. The tools neglect the effects of multiple reflections, diffraction or surface waves. The wind turbine model used in this analysis is developed with a mast as a truncated cone and not a typical cylinder [42]. The WT structure is assumed to be of perfect electric conductor material. The scattering pattern from the mast is analyzed for horizontal and vertical illumination. The red arrow in the figures following indicates the direction of the incidence.

Scattering pattern of the mast

The scattering pattern of the vertical and horizontal component of the mast is analyzed for the case when the axes are perpendicular to the illumination ($\theta_i = 90°, \phi_i = 0°$).In Fig 3.10a, the RCS of the mast is plotted for the elevation angle ($0° \leq \theta_s \leq 180°$). From the figure, the highest RCS value is in the direction perpendicular to the mast. Precisely $\theta_s = 89°$ due to the truncated structure of the mast, which results in a slightly displaced horizontal plane.

For horizontal RCS variation of the mast ($\theta_s = 90°$), for the same illumination condition as for the vertical illumination, is shown in Fig. 3.10b. A stronger forward scattering, stronger than the backward scattering, is observed and a little to no variation in azimuth angle ($270° \leq \phi_s \leq 90°$) is observed. Since this forward scattering is nearly out of phase with the incident field, it cancels each other out. This strong forward scattering will result in shadowing behind the target [43].

Scattering pattern of the wind turbine

After analyzing the impact of the mast alone from the scattering patterns in the Fig 3.10, it should be compared with the WT as a whole entity, *i.e.* the RCS of mast, nacelle, blades, and the wind turbine should be analyzed, similar to the case of the mast.

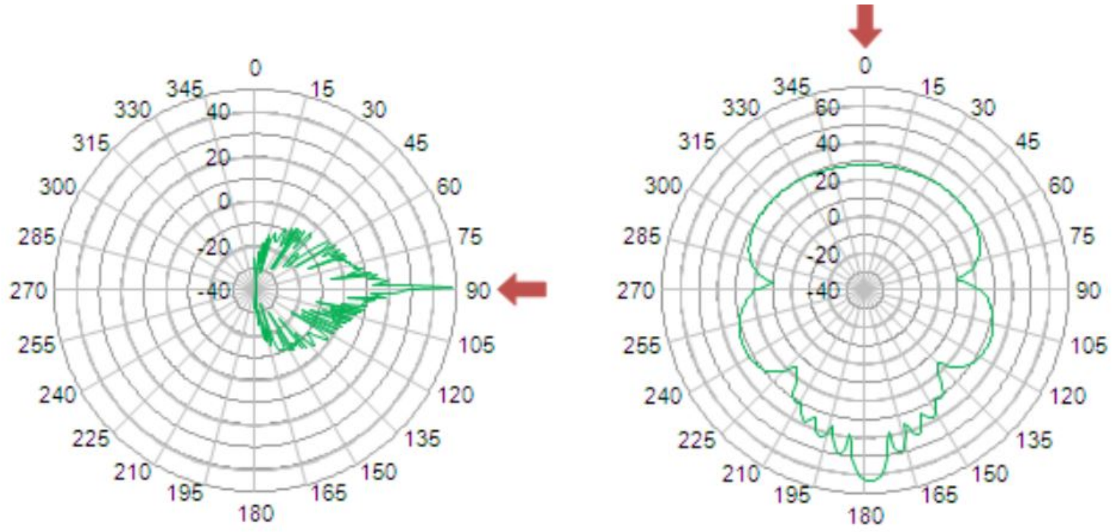

(a) (b)

Figure 3.10: Scattering pattern of the mast with perpendicular illumination ($\phi = 90°$, $\theta = 0°$) in: (a) The vertical plane ($\theta_s = 0°$) as a function of the elevation angle ϕ_s; (b) The horizontal plane ($\phi_s = 0°$) as a function of the elevation angle θ_s. The red arrow indicates the direction of incidence [9].

Fig 3.11a shows that the reflected signal is comparatively lower than the signals reflected by the WT and the blades.However, the highest value of RCS at $\theta_s = 89°$ is same as that observed for the mast. To analyze the mast contribution to the RCS of the whole wind turbine with respect to the azimuth angle ϕ_s, the RCS variation is obtained for the maximum of the vertical pattern, $\theta_s = 89°$. Hence, the results included in Fig 3.10b, instead of corresponding to the same horizontal plane, compare to the circular conical surface formed for $\theta_s = 89°$ around the WT. For horizontal scattering, it can be concluded that the RCS of the mast is significantly greater than that of the blades and nacelle.

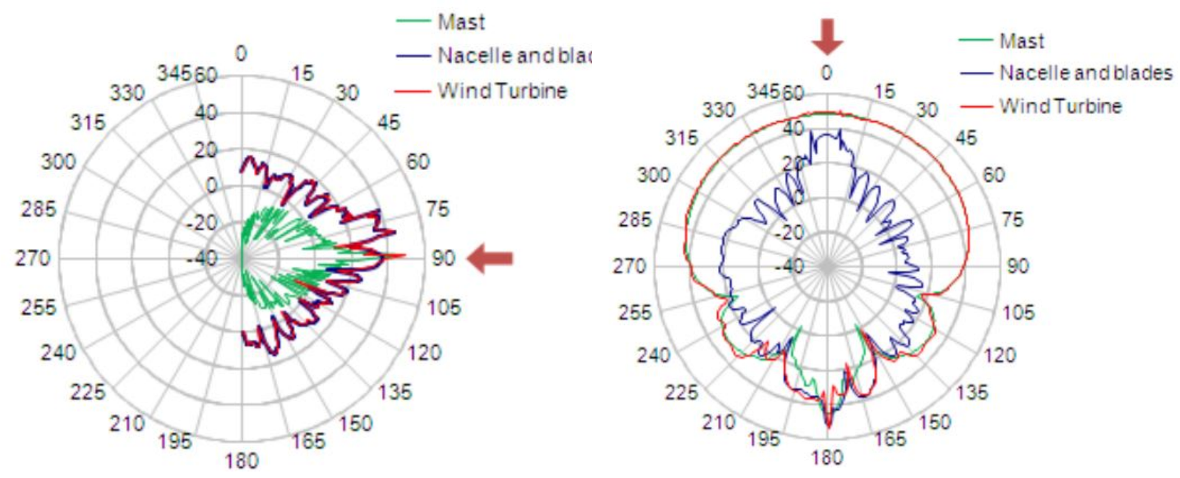

(a) (b)

Figure 3.11: Comparison of the scattering pattern of the mast, the nacelle and the blades, and the wind turbine with horizontal illumination ($\phi = 90°$, $\theta = 0°$): (a) For $\theta_s = 0°$ as a function of ϕ_s (elevation angle). (b) For $\phi_s = 89°$ as a function of θ_s(azimuth angle) [9]. The red arrow indicates the direction of incidence.

3.4. Thin Wire model

A new approach is introduced in the work of [10][8][44] using the thin wire model. The laboratory model and the software generated model have coarser results as compared to the actual results. It takes higher computational time and effort to simulate for a realistic, full-size turbine. In a new approach, [5] model the wind turbine using thin wire. Using the MoM solver in FEKO, simulations have also been carried out using thin-wire model.

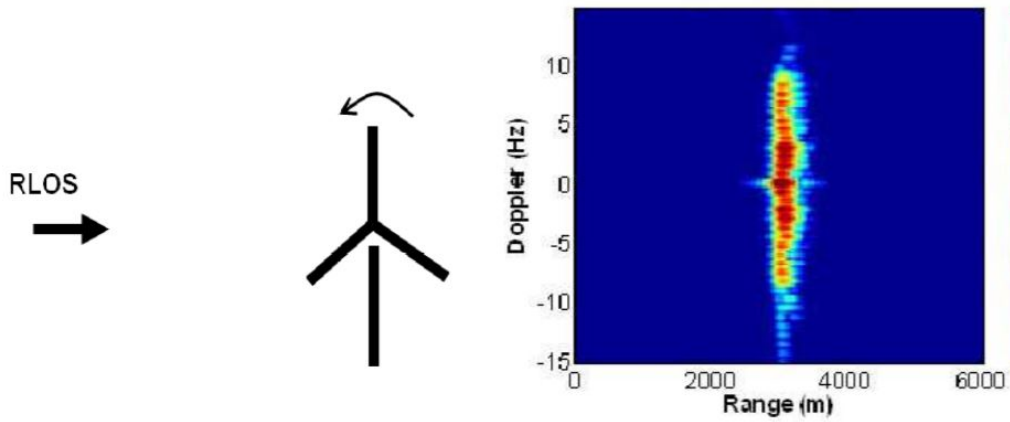

(a) (b)

Figure 3.12: Radar features of a wind turbines model using thine wire approximation in FEKO. The frequency bandwidth is 12-14MHz and the turbine rotation speed is 15rpm (a)Thin-wire model (b) Resulting spectrogram of the model [8].

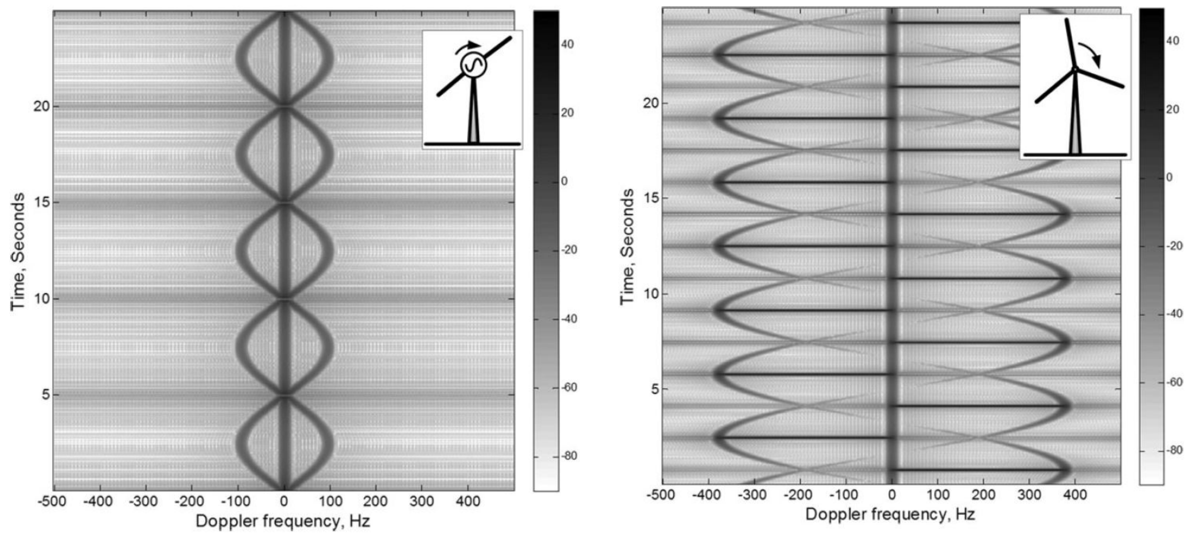

(a) (b)

Figure 3.13: The length of the wire $L = 300\lambda$, with rotation frequency $\omega = 0.1Hz$ and elevation angle $\phi_o = 0°$: (a) Amplitude Doppler Spectrogram of single linear wire; (b) Amplitude Doppler spectrogram of three linear wire replicating the structure of the wind turbine blades [10].

These simulations were carried out for High Frequency (HF) bands. The radius of the thin-wire model was assumed to be 0.26 m for λ 14 MHz, which is the maximum allowable under the thin-wire approximation ($\frac{1}{80}$). Before applying FFT, a window function (Hanning window) is applied to the frequency and aspect dimensions of the data. Fig. 3.12 shows the range-Doppler plane of a single WT. The significant feature in the data is seen at the zero Doppler bin, about the mast (or the stationary tower). The periodicity seen in the turbine signal return causes the Doppler from the blades to be spaced at 0.75 Hz, *i.e.*, three times the blades rotation 15 rpm. When the blades are vertical, the scattering centers along the blade have the maximum velocity projection onto the RLOS.

Similarly in [35], an EM model to study the radar micro-Doppler of WTs was developed using MATLAB [10]. The blades of the WTs were modeled as thin linear wire structures. To estimate the EM field radiated, the entire length of the wire structure is segmented into infinitesimal dipole of length dz'. The model was analyzed for three blades using a continuous linear frequency modulated (LFM) waveform with PRF 1kHz and a bandwidth of 10MHz.

Fig. 3.13a shows the Doppler spectrogram for one symmetric dipole antenna and Fig. 3.13b shows the spectrogram for three wire structure shifted in 120° from the preceding structure. When the dipole is at 90° with the radar line of sight (RLOS), the Doppler shift is maximum. Fig. 3.14 depicts the validation of the proposed model of the paper with the data measurement of Enercon wind turbine. The pattern simulated is very similar to the real micro-Doppler patterns.

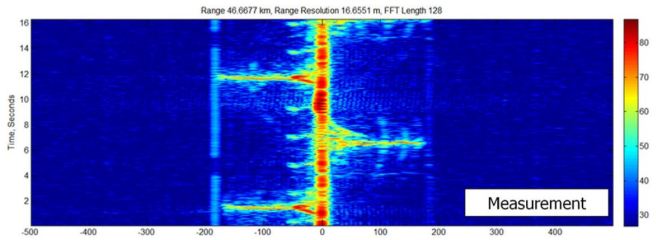

(a)

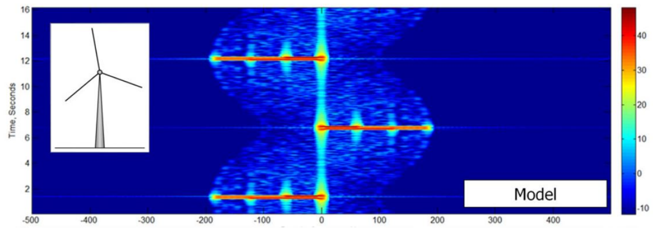

(b)

Figure 3.14: Signal decomposition to mitigate WTC; (a) Radar-Doppler signature of the collected echoes after signal processing. (b) Radar-Doppler signature of the WTC [11].

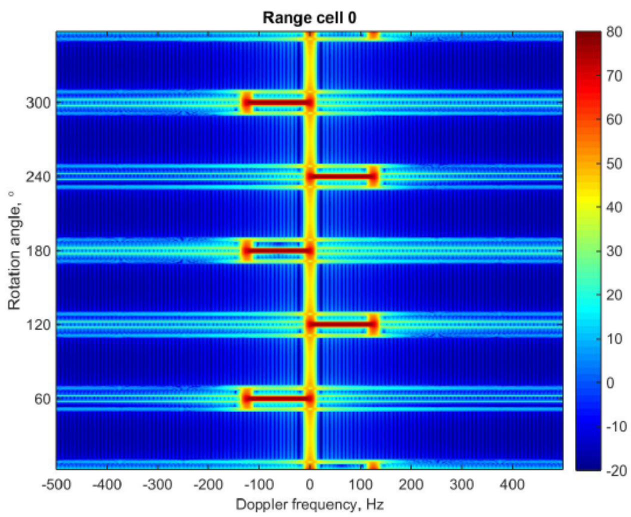

Figure 3.15: Micro-Doppler pattern of: (a) The measured data using the Enercon E82-2.3 MW WT and (b) Simulated results based on the proposed algorithm. [10].

The model proposed in [10] assumed that there is no EM coupling between different elements of the wire structures. It did not take any polarization and range resolution into account. However, this model is extended in [14] for high-resolution radar systems. The model is based on the range bin analysis. The blades of the WTs are modeled into small range cells. It assumes that the backscattering is a result of reflection from a small part of the blades and thus only a single range resolution cell is responsible for it.

In the resulting spectrogram of the simulation, there is a strong backscattering from the tip of the blades. This may be due to blade tip's overlapping in the same range cell in the same time sample as a result of range migration. Hence, resulting in a constructive and destructive interference.

3.5. Mitigation Techniques

The scattering models help in the mitigation of the WTC. The most general way to mitigate the WTC is to reduce the RCS of the WT and reduce the impact of the clutter in the radar return. Studying these clutters and their signatures helps in this process [45][46]. [11] suggested an approach to mitigate the clutter using signal

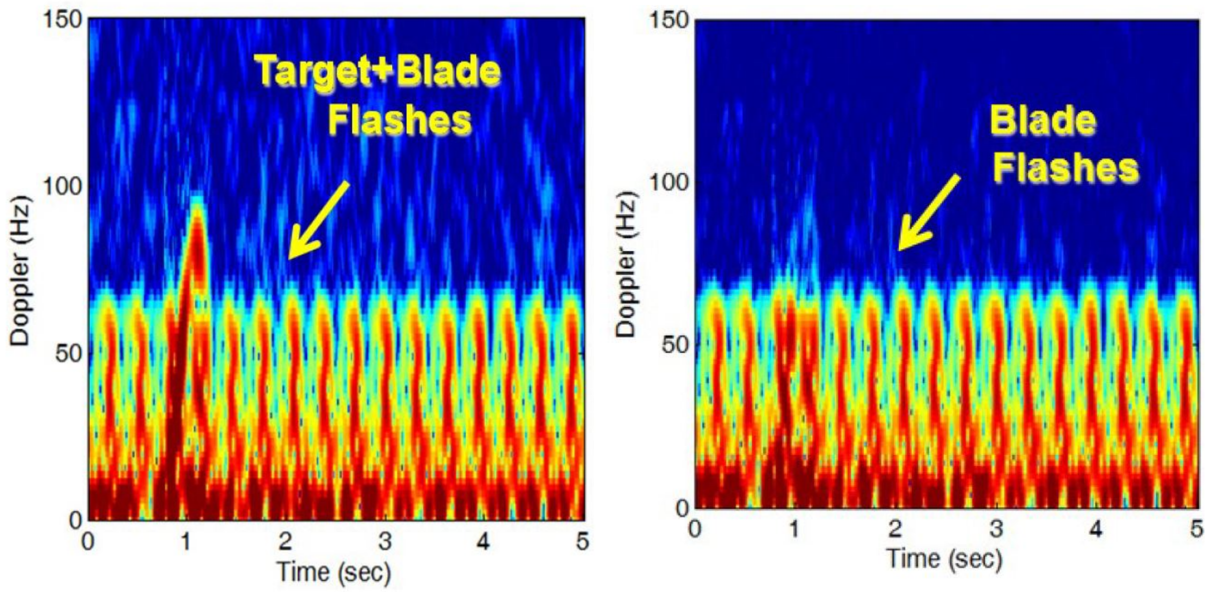

(a) (b)

Figure 3.16: Signal decomposition to mitigate WTC; (a) Radar-Doppler signature of the collected echoes after signal processing. (b) Radar-Doppler signature of the WTC [11].

decomposition. In this approach, the radar returns are decomposed into the sum of an oscillatory component and a structured transient component. The resulting spectrogram is shown in Fig 3.16. Phase and amplitude modulations need to be considered to predict the backscattering spectra from a periodically rotating structure.

3.6. Conclusion

Several models have been suggested in the literature which has been developed using the cutting-edge methods. With the growing development of wind farms and increasing demand, their impact on the radar warrant for further studies. The techniques and models highlighted in this chapter provides an insight into the prevailing knowledge on this subject. However, there are certain topics of concern pertaining to complex and time-consuming algorithms. Also, there has been no focus on the phase difference of the radar returns. These issues have paved a way to further improve the shortcoming of these models. These shortcomings are the motivation of the present study. The proposed model is discussed in detail in the following chapters.

4

Model Design

In the previous chapter, various approaches and the models in literature dealing with WT scattering were addressed. The main limitation associated with those models were the complexities, may it be the design complexity or computational complexity. To overcome these complexities, this chapter introduces a simplified model of a wind turbine which is developed using the thin-wire approximation. The present chapter will provide an overview regarding the design and methods included in developing the EM model proposed in this thesis. It also involves a brief description of the general design of a wind turbine.

4.1. Wind Turbines Design

The design of the EM model for the WT is based on the architecture of horizontal-axis wind turbines (HAWT). A HAWT is a type of wind turbine that has the main rotor shaft and an electrical generator mounted on the top of a tower, typically comprising a nacelle, a hub, a tower, and the rotor blades as shown in Fig. 4.1. The tower generally is made of thick steel. The gearbox, generator, and the main frame comprises the nacelle and contribute to most of the wind turbine clutters (WTC). However, the WTC from these parts can be filtered out using ground clutter mitigation methods because of their stationary nature compared to the rotation and micro-motion of the WT blades.

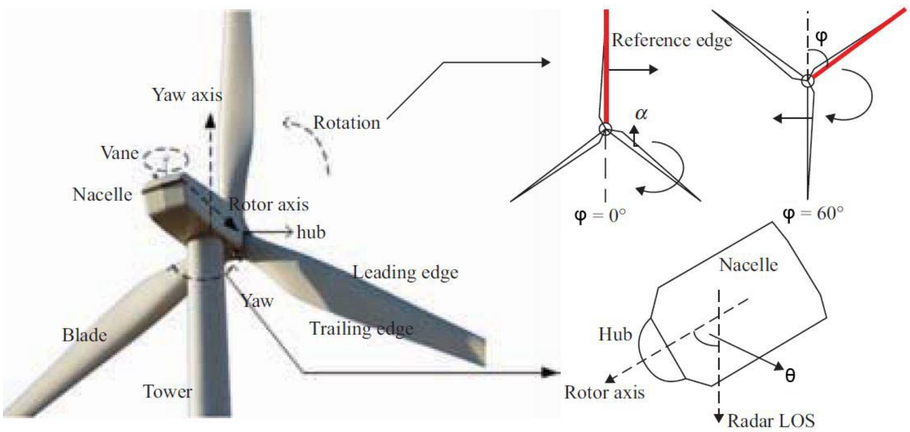

Figure 4.1: Horizontal axis wind turbine structure along with their orientation nomenclature [7].

The WT blades typically rotate clockwise as viewed from the front view. The leading edge of the blades has a thicker edge than the trailing edge. The WTB designs have been elaborated in detail in [36]. The position of the blades, denoted by ϕ ($0° \le \phi < 360°$), is the angle displaced by the reference leading edge from the vertical position. The aspect angle θ ($0° \le \theta < 360°$) is the angle between the RLOS and the rotor axis.

4.2. EM Design of the model

In Chapter 3, various models of the WT, scaled model (Section 3.2.1) or software models (Section 3.3) have been discussed, but the results show some deviations from the real-time observations [47][48]. The recent approaches focus on high-frequency approximation such as microwave optics and PO (Section 3.3), that solely deals with the RCS of the WT. Additionally, PO does not account for surface wave propagation, affecting the accuracy of the model [6]. As for the software models, they result in high computational time especially for large structures like the WT. Computational methods like MoM are limited by their low frequency approximations [49]. The theoretical models often deals with the RCS with no regard to the phase differences of the radar returns. Additionally, most of the works are often concentrated around high microwave regime („1 GHz) and HF bands.

The primary EMI problems of WTS can be formulated as how accurately the current distribution over the entire structure and its radiation fields can be estimated based on various EM excitations. Some of these excitation sources include incident waves from radar/communication transmitters, transient lighting electric fields, and radiations from internal electronics. Although, numerous solutions have been proposed to curb these issues, most of the approaches are either empirical or operational. Moreover, WTS interaction with EM fields has been very limited.

In this thesis, a new approach to study the scattering of radar signals from WT is introduced. It is focused on the VHF (30 to 300 MHz, wavelength λ_{VHF} of 1-10m) and UHF (300 MHz to 3 GHz, wavelength λ_{UHF} of 1m-1dm) bands. The impact of atmospheric noise and interference from the electrical components is lesser in VHF as compared to lower frequencies. The wind turbine blades are modeled as linear wire structures. The WT model attempts to overcome the computation effort and processing time as a consequence of the complex algorithms and models. The model is reasonably simplified compared to its contemporary models but it is still able to predict and give a result close to the practical observation, as validated later in Chapter 6.

The model was first designed for mono-static case (Section 6.1), including the polarization and the aspect angle. The bi-static case (Section 4.3) has also been included in the model. Consequently, the impact of the mast (Section 4.3.1) was further added into the model. In Chapter 2, the concept of mono-static scattering was defined. In the following section, the design of mono-static scattering will be discussed. Throughout the model, it is assumed that the incident wave is a plane EM wave.

4.2.1. Model Design for Mono-Static Scattering on WT

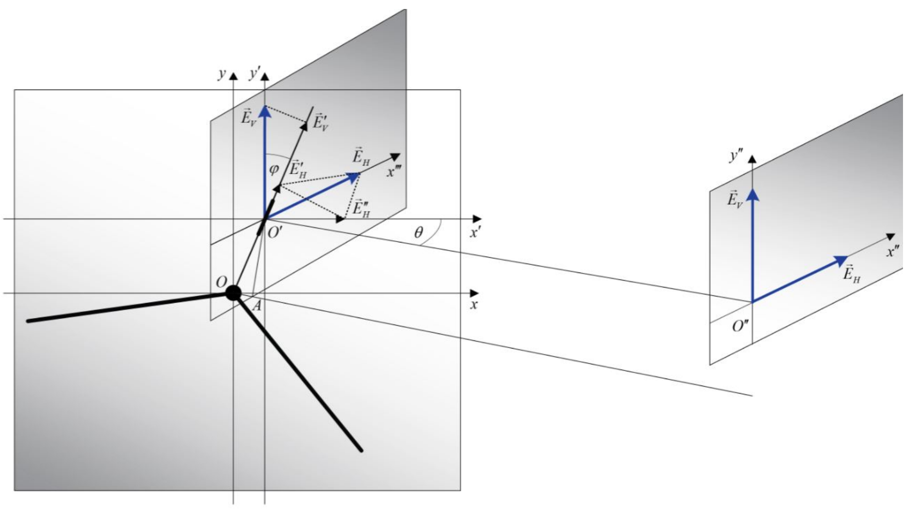

Figure 4.2: Geometric Representation of the fields. ϕ denotes the orientation angle of the WTBs in the rotation plane, and ϕ denotes the aspect angle.

In the work done in [10][14], the blades of the WTs are modeled as finite length linear wires, where the radius of the wires a is minimal in comparison to its length L ($a \ll L$). For thin-wire approximation, it assumed that the current in the wire is restricted to the direction of the wire and uniform along the cross-section of the wire.

Consider a coordinate system (O = x, y, z) and a dipole with thin-wire approximation [50]. The center of rotation of the WT is placed at the origin of the coordinate system as shown in Fig. 4.2. The finite length dipole is sub-divided into a number of infinitesimal dipole length of dz'. The dipole is at placed at $O' = x', y', z'$ which is at a distance z' ∈ $\lfloor 0,\mathrm{L} \rfloor$ from o' . The radar is at a coordinate (x'', y'', z'') where the $x'' - y''$ plane is at an aspect angle θ with the plane of rotation $(x' - y')$ at a fixed distance of z_o =1.5 km.

From [50], the electric field from all the infinitesimal elements over the wire length L is given by

$$E_\phi = \int_L dE_\phi = j\eta \frac{ke^{-jkz_o}}{4\pi z_o} \sin\phi \left[\int_L I_e(x', y', z') e^{jkz'\cos\phi} dz' \right] \tag{4.1}$$

where $j\eta \frac{ke^{-jkr}}{4\pi z_o} \sin\phi$ and $\int_L I_e(x', y', z') e^{jkz'\cos\phi} dz'$ are known as *element factor* and *space factor* respectively. The term z_o is the distance between the center of the coordinates and the observation point. The space factor is a function of the current distribution along the linear wire structure.

The observation was done for 0° aspect/azimuth angle in the previous works which implies that the radar line of sight (RLOS) and the rotation plane of the wind turbine blades (WTB) are parallel. In this case, the resulting back-scattered field is proportional to

$$dE_\phi^{BS}(\phi, z') \sim j\eta \frac{ke^{-jkz_0}}{4\pi z_0} E_\phi(r) \sin^2\phi e^{+j2kz'\cos\phi} dz' \tag{4.2}$$

To extend the model into a 3-D model, the condition of ϕ (0° < ϕ < 360°) should be realized. Then, the resulting back-scattered field can be calculated using the Fig 4.2.

$$E_{VV}^S = E_V \cos^2\phi(t) \tag{4.3}$$

$$E_{HH}^S = E_H \sin\theta \sin\phi(t) \tag{4.4}$$

From Fig. 4.2, the displacements of the components from the rotation center where L is the length of the WT blades is given by

$$\Delta R_{VV}^S = L\cos\theta \sin\phi(t) \tag{4.5}$$

$$\Delta R_{HH}^S = \Delta R_{VV}^R \tag{4.6}$$

Using these relations, the following equations for the back-scattered field can be derived

$$dE_{VV}^{BS}(\phi(t), \theta, z') \sim j\eta \frac{ke^{-jkz_0}}{4\pi z_0} E_V \cos^2\phi(t) e^{+j2kz'\sin\phi(t)\cos\theta} dz' \tag{4.7}$$

$$dE_{V+H}^{BS}(\phi(t), \theta, z') \sim j\eta \frac{ke^{-jkz_0}}{4\pi z_0} E_V \cos\phi(t) \sin\phi(t) \sin\theta e^{+j2kz'\sin\phi(t)\cos\theta} dz' \tag{4.8}$$

$$dE_{HH}^{BS}(\phi(t), \theta, z') \sim j\eta \frac{ke^{-jkz_0}}{4\pi z_0} E_H \sin^2\theta \sin^2\phi(t) e^{+j2kz'\sin\phi(t)\cos\theta} dz' \tag{4.9}$$

$$dE_{H+V}^{BS}(\phi(t), \theta, z') \sim j\eta \frac{ke^{-jkz_0}}{4\pi z_0} E_H \sin\theta \sin\phi(t) \cos\phi(t) e^{+j2kz'\sin\phi(t)\cos\theta} .dz' \tag{4.10}$$

Putting the equations in the polarization scattering matrix, $S(\phi, \theta, z')$ (Section 2.6) is given by

$$\begin{bmatrix} E_V^S \\ E_H^S \end{bmatrix} = A(z') \begin{bmatrix} S_{VV} & S_{VH} \\ S_{HV} & S_{HH} \end{bmatrix} \begin{bmatrix} E_V^T \\ E_H^T \end{bmatrix} \tag{4.11}$$

$$dS(\phi, \theta, z') = A(z') \begin{bmatrix} \cos^2\phi(t) & \cos\phi(t)\sin\phi(t)\sin\theta \\ \cos\phi(t)\sin\phi(t)\sin\theta & \sin^2\phi(t)\sin^2\theta \end{bmatrix} dz' \tag{4.12}$$

where

$$A(z') = j\eta \frac{e^{-jkz_0}}{4\pi z_0} . e^{+j2kz' \sin\phi(t)\cos\theta} \tag{4.13}$$

The total electric field can be calculated by integrating $dS(\phi,\theta,z')$ over the total length of the blade L as follows

$$\mathbf{E}^S = \Big\{ \sum_{n=1}^{3} \int_0^L \mathbf{S}(\phi + \Delta\phi_n, \theta, z') dz' \Big\} \mathbf{E}^\mathbf{T} \tag{4.14}$$

where $\phi_n = -120°, 0, 120°$ for $n = 1,2,3$ is the difference in the orientation angles between blades.

When the blade is perpendicular to RLOS, or vertical when radar elevation angle is small, the blade is aligned with the tower. This alignment may lead to constructive in-phase coherent integration of backscattered EM field that results in stronger radar return. However, due to the rotation of the blade, this in-phase does not last long and the scattering points have range shifting in scales comparable to radar wavelength causing significant oscillations. Because of this, the peak of interference drops rapidly and starts oscillating [7].

4.3. Model Design for Bi-Static Scattering on WT

The bi-static model set-up is illustrated in Fig. 4.3. θ represents the aspect angle, and ϕ represents the blade's displacement position from the vertical plane in the equations. For the proposed model design, the reflection from the ground plane is ignored. The mathematical representation of the fields can be derived using Fig 4.3.

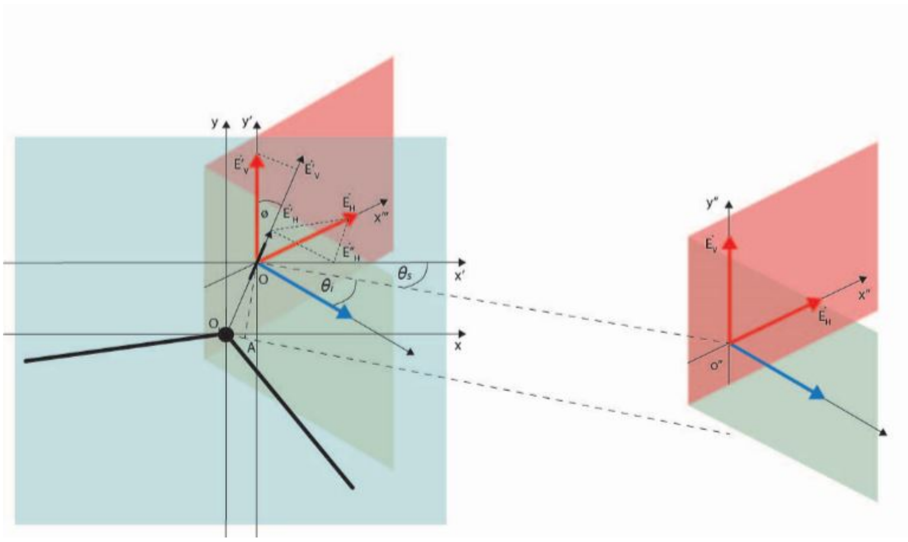

Figure 4.3: Geometric representation of the bi-static model design of the wind turbine blades (WTB).The red plane denotes the scattering plane, and the green plane denotes the plane of the incident wave; the blue plane denotes the plane of rotation (POR) of the WTBs depending on the aspect angle or azimuth angle θ. θ_i and θ_s denote the angle between the POR, and the plane of incident wave and scattered wave respectively. The reflection from the ground plane is ignored.

The coordinates are similar to the mono-static scattering model design (Section 6.1). However, the plane of the incident signal is different from the plane of the scattering signal. The angle between the incident angle and the scattered angle is known as the bi-static angle.

The equations for the projections of incident field polarization components on WT wire model structure are as follows

$$E_{VV} = E_V \cos^2 \phi(t) \tag{4.15}$$

$$E_{HH} = E_H \sin^2 \phi(t) \sin\theta_s \sin\theta_i \tag{4.16}$$

$$E_{HV} = E_H \sin\phi(t)\cos\phi(t)\sin\theta_i \tag{4.17}$$

$$E_{VH} = E_V \cos\phi(t)\cos\phi(t)\sin\theta_s \tag{4.18}$$

where the subscripts i and s represents the incident and scattering azimuth angle respectively.

The direction of propagation of the incident and the scattered field is different. The phase difference between the rotation center and the element of WTS at the distance z' from the rotation center can be evaluated as

$$\Delta\phi = k(\Delta z_i + \Delta z_s) = kz' \sin\phi(t)(\cos\theta_i + \cos\theta_s) \tag{4.19}$$

where

$$\Delta z_i = z' \sin\phi(t)\cos\theta_i$$

$$\Delta z_s = z' \sin\phi(t)\sin(90-\theta_i) = z' \sin\phi(t)\cos(\theta_S)$$

Using the above derivation, the following equations for the back-scattered field are

$$dE^{BS}_{VV}(\phi(t),\theta,z') \sim j\eta \frac{ke^{-jkz_0}}{4\pi z_0} E_V \cos^2\phi(t) e^{+jkz'\sin\phi(t)(\cos\theta_i+\cos\theta_s)} dz' \tag{4.20}$$

$$dE^{BS}_{V+H}(\phi(t),\theta,z') \sim j\eta \frac{ke^{-jkz_0}}{4\pi z_0} E_V \cos\phi(t)\cos\phi(t)\sin\theta_s e^{+jkz'\sin\phi(t)(\cos\theta_i+\cos\theta_s)} dz' \tag{4.21}$$

$$dE^{BS}_{HH}(\phi(t),\theta,z') \sim j\eta \frac{ke^{-jkz_0}}{4\pi z_0} E_H \sin^2\phi(t)\sin\theta_s \sin\theta_i e^{+jkz'\sin\phi(t)(\cos\theta_i+\cos\theta_s)} dz' \tag{4.22}$$

$$dE^{BS}_{H+V}(\phi(t),\theta,z') \sim j\eta \frac{ke^{-jkz_0}}{4\pi z_0} E_H \sin\phi(t)\cos\phi(t)\sin\theta_i e^{+jkz'\sin\phi(t)(\cos\theta_i+\cos\theta_s)} .dz' \tag{4.23}$$

Putting the equations in the matrix, $S(\phi,\theta,z')$ can be represented as follows

$$\begin{bmatrix} E^R_V \\ E^R_H \end{bmatrix} = \begin{bmatrix} S_{VV} & S_{VH} \\ S_{HV} & S_{HH} \end{bmatrix} \begin{bmatrix} E^T_V \\ E^T_H \end{bmatrix} \tag{4.24}$$

$$dS(\phi,\theta,z') = A(z') \begin{bmatrix} \cos^2\phi(t) & \sin\phi(t)\cos\phi(t)\sin\theta_i \\ \sin\phi(t)\cos\phi(t)\sin\theta_s & \sin^2\phi(t)\sin\theta_s\sin\theta_i \end{bmatrix} dz' \tag{4.25}$$

where

$$A(z') = j\eta \frac{e^{-jkz_0}}{4\pi z_0} .e^{+jkz'\sin\phi(t)(\cos\theta_i+\cos\theta_s)} \tag{4.26}$$

The total electric field is found by integrating $S(\phi,\theta,z')$ over the total length of the dipole L as follows

$$\mathbf{E^s} = \sum_{n=1}^{3} \int_0^L \mathbf{S}(\phi + \Delta\phi_n, \theta, z') dz' \tag{4.27}$$

where $\phi_n = -120°, 0°\&120°$ for $n = 1,2,3$ is the difference in the orientation angle between the n blades.

4.3.1. Mast influence

In the literature review section 3.3, the influence of mast in the WT was highlighted. However, in the literature the study has been done on the basis of the RCS of the cylinder. In this thesis, in order to study the mast contribution in the EM model , the bi-scattering matrix is derived for a finite length dielectric cylinder with a vertical orientation from [12].

The tower/mast is modeled as a cylinder of radius a with a height of L_{hub}. The technical data for the tower and the blades for the wind turbine simulations is taken from the Lagerwey WT.

Fig 4.4 represents the cylinder alignment for an arbitrary orientation. For the vertical case, θ_c and ϕ_c are equal to zero. The unit vector along the axis of the cylinder is given by

$$\mathbf{c}(\theta_c,\phi_c) = \sin\phi_c\cos\theta_c\mathbf{x} + \sin\phi_c\sin\theta_c\mathbf{y} + \cos\phi_c\mathbf{z} \tag{4.28}$$

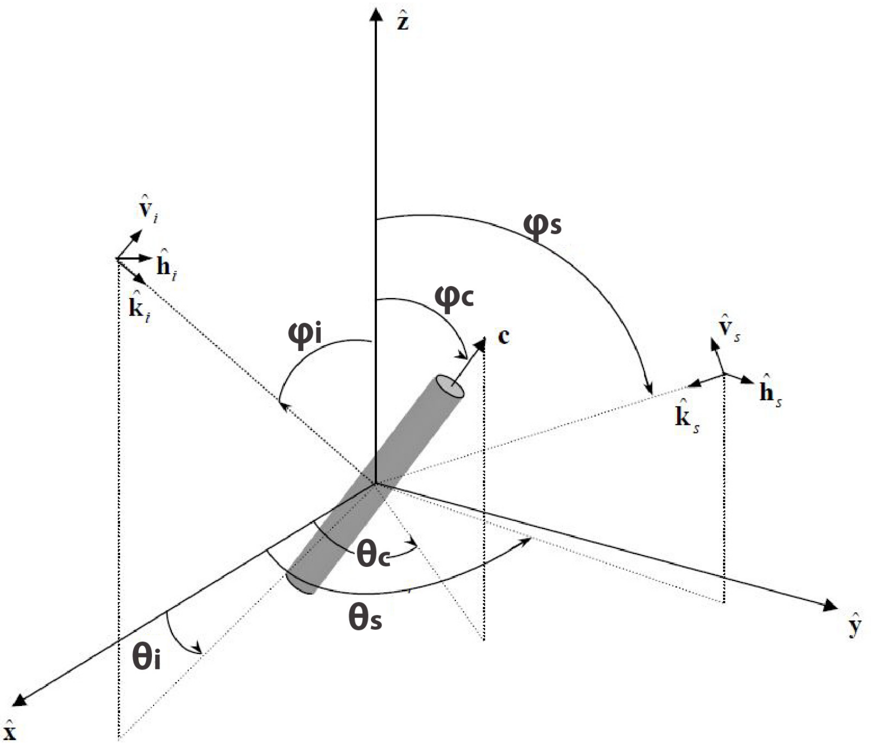

Figure 4.4: Geometric Representation of the global alignment of the cylinder in the co-ordinate system [12].

For the scattered field, the propagation vector is represented by

$$\mathbf{k_s} = -\sin\phi_s\cos\theta_s\mathbf{x} - \sin\phi_s\sin\theta_s\mathbf{y} - \cos\theta_s\mathbf{z} \tag{4.29}$$

Thus, from 4.28 and 4.29, the dot product is given by

$$\mathbf{k_s.c} = -\cos\phi_s \tag{4.30}$$

Also,

$$\begin{aligned} D^e = &\sum_{m=-\infty}^{+\infty}(-1)^m J''_m(x_0)\Big\{J_m(y_0) - \tfrac{\sin\phi_i}{B}J_m(x_0)J'_m(y_0) \\ &+C_m^{TM}\Big[H_m^{(1)\prime}(x_0)J_m(y_0) - \tfrac{\sin\phi_i}{B}H_m^{(1)\prime}(x_0)J'_m(y_0)\Big] \\ &+\tfrac{m\cos\phi_i}{x_0}\left(1 - \tfrac{\mathbf{k}_s.\mathbf{c}(0,0)}{\cos\phi_i}\tfrac{x_0\sin\phi_i}{y_0 B}\right)\bar{C}_m H_m^{(1)}(x_0)J_m(y_0)\Big\}e^{im\tilde{\theta}} \end{aligned} \tag{4.31}$$

$$\begin{aligned} D^h = &\sum_{m=-\infty}^{+\infty}(-1)^m \Big\{J''_m(x_0)J_m(y_0) - \tfrac{\sin\phi_i}{B}J_m(x_0)J'_m(y_0) \\ &+C_m^{TE}\Big[H_m^{(1)\prime}(x_0)J_m(y_0) - \tfrac{\sin\phi_i}{B}H_m^{(1)\prime}(x_0)J'_m(y_0)\Big] \\ &+\tfrac{m\cos\phi_i}{x_0}\left(1 - \tfrac{\mathbf{k}_s.\mathbf{c}(0,0)}{\cos\phi_i}\tfrac{x_0\sin\phi_i}{y_0 B}\right)\bar{C}_m H_m^{(1)}(x_0)J_m(y_0)\Big\}e^{im\tilde{\theta}} \end{aligned} \tag{4.32}$$

$$\begin{aligned} \bar{D}^e = &\sum_{m=-\infty}^{+\infty}(-1)^m e^{im\tilde{\phi}}\Big\{\bar{C}_m\Big[H_m^{(1)\prime}(x_0)J_m(y_0) - \tfrac{\sin\phi_i}{B}H_m^{(1)}(x_0)J'_m(y_0)\Big] \\ &+\tfrac{m\cos\phi_i}{x_0}\left(1 - \tfrac{\mathbf{k}_s.\mathbf{c}(0,0)}{\cos\phi_i}\tfrac{x_0\sin\phi_i}{y_0 B}\right)\Big[J_m(x_0) + C_m^{TE}H_m^{(1)}(x_0)\Big]J_m(x_0)\Big\} \end{aligned} \tag{4.33}$$

$$\begin{aligned} \bar{D}^h = &\sum_{m=-\infty}^{+\infty}(-1)^m e^{im\tilde{\phi}}\Big\{\bar{C}_m\Big[H_m^{(1)\prime}(x_0)J_m(y_0) - \tfrac{\sin\phi_i}{B}H_m^{(1)}(x_0)J'_m(y_0)\Big] \\ &+\tfrac{m\cos\phi_i}{x_0}\left(1 - \tfrac{\mathbf{k}_s.\mathbf{c}(0,0)}{\cos\phi_i}\tfrac{x_0\sin\phi_i}{y_0 B}\right)\Big[J_m(x_0) + C_m^{TM}H_m^{(1)}(x_0)\Big]J_m(x_0)\Big\} \end{aligned} \tag{4.34}$$

$$B = \frac{1}{2}\sqrt{(\sin\phi_i + \sin\phi_s\cos(\theta_s-\theta_i))^2 + \sin^2\phi_s\cos^2(\theta_s-\theta_i)^2} \tag{4.35}$$

where

$$\begin{aligned}\cos\tilde{\theta} &= \tfrac{1}{2B}(\sin\phi_s\cos(\theta_s-\theta_i)+\sin\phi_i)\\ \sin\tilde{\theta} &= \tfrac{1}{2B}\sin\phi_s\sin(\theta_s-\theta_i)\end{aligned} \tag{4.36}$$

$$\begin{aligned}y_0 &= k_0 a B\\ x_0 &= k_0 a\sin\phi\end{aligned} \tag{4.37}$$

$$C_m^{TM} = -\frac{V_m P_m - q_m^2 J_m(x_0) H_m^{(1)}(x_0) J_m^2(x_1)}{P_m N_m - \left[q_m H_m^{(1)}(x_0) J_m(x_1)\right]^2} \tag{4.38}$$

$$C_m^{TE} = -\frac{M_m N_m - q_m^2 J_m(x_0) H_m^{(1)}(x_0) J_m^2(x_1)}{P_m N_m - \left[q_m H_m^{(1)}(x_0) J_m(x_1)\right]^2} \tag{4.39}$$

$$\bar{C}_m = i\frac{2}{\pi x_0\sin\phi_i}\frac{q_m J_m^2(x_1)}{P_m N_m - \left[q_m H_m^{(1)}(x_0) J_m(x_1)\right]^2} \tag{4.40}$$

with

$$x_1 = k_0 a\sqrt{\varepsilon - \cos^2\phi_i} \tag{4.41}$$

$$q_m = m k_0 a\cos\phi_i\left(\frac{1}{x_1^2} - \frac{1}{x_0^2}\right) \tag{4.42}$$

$$V_m = k_0 a\left\{\frac{\varepsilon}{x_1} J_m(x_0) J'{}_m(x_1) - \frac{1}{x_0} J''{}_m(x_0) J_m(x_1)\right\} \tag{4.43}$$

$$P_m = k_0 a\left\{\frac{1}{x_1} H_m^{(1)}(x_0) J'{}_m(x_1) - \frac{1}{x_0} H_m^{(1)\prime}(x_0) J_m(x_1)\right\} \tag{4.44}$$

$$N_m = k_0 a\left\{\frac{\varepsilon}{x_1} H_m^{(1)}(x_0) J'{}_m(x_1) - \frac{1}{x_0} H_m^{(1)\prime}(x_0) J_m(x_1)\right\} \tag{4.45}$$

$$M_m = k_0 a\left\{\frac{1}{x_1} J_m(x_0) J'{}_m(x_1) - \frac{1}{x_0} J'{}_m(x_0) J_m(x_1)\right\} \tag{4.46}$$

Substituting all the above equations from 4.31 - 4.46, the scattering matrix of a cylinder with vertical orientation can be simplified as

$$S_{hh}(\theta_i,\phi_i,\theta_s,\phi_s) = -\frac{1}{2}\frac{k_0 a l}{\sin\theta_i}\frac{\sin(k_0 l(\cos\theta_i+\cos\theta_s)/2)}{k_0 l(\cos\phi_i+\cos\phi_s)/2} D^h \tag{4.47}$$

$$S_{hv}(\theta_i,\phi_i,\theta_s,\phi_s) = -\frac{1}{2}\frac{k_0 a l}{\sin\phi_i}\frac{\sin(k_0 l(\cos\phi_i+\cos\phi_s)/2)}{k_0 l(\cos\phi_i+\cos\phi_s)/2} i\bar{D}^h \tag{4.48}$$

$$S_{vh}(\theta_i,\phi_i,\theta_s,\phi_s) = +\frac{1}{2}\frac{k_0 a l}{\sin\phi_i}\frac{\sin(k_0 l(\cos\phi_i+\cos\phi_s)/2)}{k_0 l(\cos\phi_i+\cos\phi_s)/2} i\bar{D}^e \tag{4.49}$$

$$S_{vv}(\theta_i,\phi_i,\theta_s,\phi_s) = -\frac{1}{2}\frac{k_0 a l}{\sin\phi_i}\frac{\sin(k_0 l(\cos\phi_i+\cos\phi_s)/2)}{k_0 l(\cos\phi_i+\cos\phi_s)/2} D^e \tag{4.50}$$

where
a = Radius of the cylinder,
$k_0 = \frac{2\pi}{\lambda}$ is the wave number of the incident wave, and
l = Length of the cylinder.

Since the bi-scattering matrix is already calculated in section 4.3, the resulting S-matrix of the wind turbine can be calculated as

$$S_{WT} = S_M e^{jk\Delta z} + S_{\text{BiScattering}} \tag{4.51}$$

and

$$\Delta z = \cos\phi_s L_{nacelle}$$

where S_{WT},S_M, and $S_{\text{BiScattering}}$ represents the scattering matrix of the wind turbine, mast, and the bi-scattering matrix respectively, and Δz is the path difference from the plane of rotation of the blades to the center of the mast. The scattered field $\mathbf{E}^{sc}$ can then be calculated using the relation with $\mathbf{E}^{inc}$ as

$$\mathbf{E}^{sc} = S_M \mathbf{E}^{inc} \frac{e^{ikr}}{r} \tag{4.52}$$

4.4. Range Profiling of WT Radar Response

In Section 2.2, the concept of stepped frequency and pulse compression were explained. The stepped frequency given by 2.9 and 2.10 can be written as

$$f_n = f_o - \frac{B}{2} + \frac{B}{n} N \tag{4.53}$$

where Δf and f_n is the frequency step size and carrier frequency at the n^{th} pulse respectively.

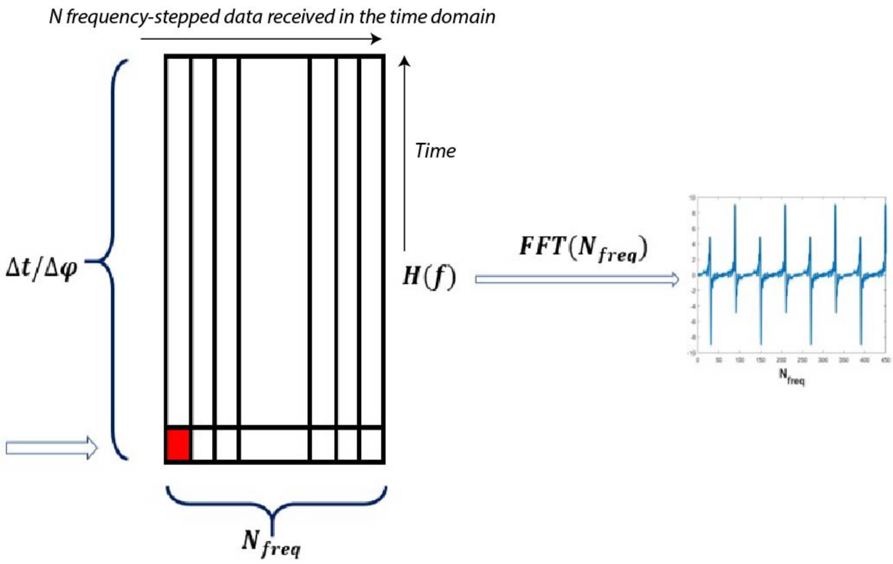

Figure 4.5: Illustration of range profile in the proposed model to understand the WT response. N_{freq} is the number of pulses.

In the proposed model, the radar transmits a stepped frequency waveform using pulse compression to achieve high resolution results. Fig. 4.5 illustrate the time and frequency relation of the stepped frequency radar return. To obtain the range profile of the signal return from the radar, the FFT is applied to the time series to obtain the range profile in frequency domain. $\phi(t)$ is rotation degree which is function of time. The reflected signal received by the radar is then sampled at a rate of PRF. For simplification, it is assumed the target lies in the range $[-R_0, R_0]$ with

$$R_0 = \frac{cA}{2(N-1)\Delta f} = \frac{cA}{2B}$$

where $A \in \left[-\frac{N}{2}, \frac{N}{2}\right]$.

4.5. Conclusion

A theoretical model with simplified approach has been developed in this chapter. The thin-wire model was designed for both mono-static scattering and bi-static scattering cases. The model also includes the influence of the mast in the reflected signal from the radar. Unlike the models in the literature, the proposed model takes into account the polarization and the phase difference between the signals. The results from the model, which will be addressed in the following chapter, validate the credibility of this model.

5

Model Validations

In the previous chapters, the existing state of the art, the development of the theoretical models, *etc*. were discussed. In such non-empirical models, there is need to ensure it has some credibility.

How can this model be validated to make it more accountable ?

In order to prove its credibility, the results of the theoretical model need to be validated with a real-time data. In this thesis, the validation of the results of the model will be done using data measured by the Agentschap Telecom, the Netherlands. Thus, with the help of the measurement data, it was possible to quantify the similarity between their data and the present model. This chapter will explain how the experiment was set up and the measurements that were carried out to acquire the data which were used to validate the proposed model.

5.1. Introduction

In 2015, the Radio-communications Agency surveyed the influence of the wind turbines on the broadcast signal reception. This was done based on the assumptions of the radar cross section (RCS) of the wind turbines. The reason for this is that there is, in general, little or no measurement results about RCS of (large) wind turbines are known at frequencies below 1 GHz.

The report [13] with the measurement data, describes the implementation and results of measurements of the radar cross-section of a wind turbine test site in Lelystad, on April 4, 17 May, and 16 June 2016. The report with the measurements as reported was provided by the Agentschap Telecom [13].

5.2. Measurement Technique

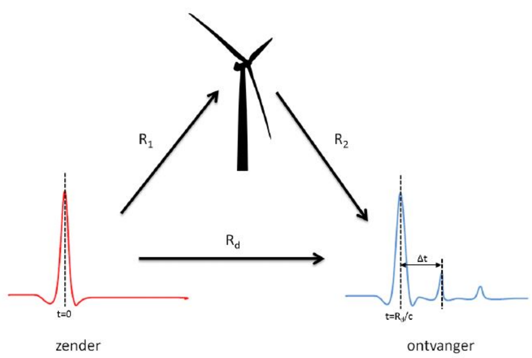

Figure 5.1: The transmission and reception of a short duration pulse [13].

For the determination of the radar cross section (RCS) of a wind turbine, an amount of high-frequency energy is sent in the direction of the wind turbine, and it is measured how much of this energy is received due to reflection from the WT. For this, a measurement performed on one type of WT, in a bi-static arrangement, at a fixed angle of reflection for a single frequency.

In the execution of the measurement, it must be taken into account that at the receiver the signal R_d both $R_1 + R_2$ arrives in two ways as illustrated in Fig. 5.1. One is through direct transmission at LOS and another is transmitted via the WT. In addition, there will be reflections from other objects from the surrounding environment. Therefore, it is important to know which reflection has been specifically derived from the desired object.

In Fig 5.1, a pulse which is emitted at $t = 0$ reaches the receiver through direct propagation and propagation via the WT. The time taken by the pulse to reach the receiver via the direct path R_d is

$$t = \frac{R_d}{c} \tag{5.1}$$

where c is the speed of light and R_d is the distance between the receiver and transmitter. The reflected pulse via the wind turbine will take longer and receive the signal after a time difference Δt. This time difference depends on the difference in path length and is given by

$$\Delta t = \frac{R_1 + R_2 - R_d}{c}. \tag{5.2}$$

If the difference in path length is known, then the signal with the time difference of Δt can be determined as the pulse which propagated via the WT. In this way, the reflection of the object of interest to be measured can be distinguished from signals reflected by other objects or clutters. The received power of the reflected pulse is then a measure of the radar cross-section of the wind turbine.

It should be noted that due to the large dimension of the wind turbine structure (WTS), near-field effects should be taken into account for measurements carried out at a short distance. To better understand the influence of near-field impact, the measurements are carried out in different distances as shown in Fig. 5.2.

5.3. Measurement Set Up

Figure 5.2: Measurement set-up at the test site Lelystad. The red dot represents the target (WT), the yellow and the blue circles represents the receiver and the transmitters respectively.

The measurement set up placed in Lelystad is as shown in the Fig. 5.2 and the equipment used are shown in Fig. 5.3. The wind turbine is the target of interest indicated as "Lagerwey" (red circle) in the image. The receivers are marked R1-R6 and the transmitters are marked T1-T3. There are two other neighboring WTS

(Enercon 1 and Enercon 2). considering their sheer size, these structures can cause strong reflections. The distance between the Tx and Rx are 1 km, 2 km, and 4 km respectively. The receiver and the transmitter are placed at right angles from each other. The table summarizes the parameters indicated in the image.

Parameter	Item in image
Frequency MHz	200,280,605,60
Target	Lagerway
Transmitter	T1 T2 T3
Receiver	R1 - R6
Wind Turbines	Enercon 1 and 2

Table 5.1: Explanation of parameters in Fig. 5.2.

The measurements were done for three different configurations. They are tabulated in the table below.

Configuration	Distance
T1-R1	1 km
T2-R2	2 km
T3-R3	4 km

Table 5.2: Different configurations of the measurement set up.

Figure 5.3: Measurement set-up of the sender, wind turbine, and the receiver respectively

5.4. Results

The numerical results of the measurements are tabulated in Table 5.3 Due to the limitation of the measurement set up, the performance of the equipment were not meaningful for greater distances. The deviations from the calculated to measured values are also tabulated. The different configurations were studied for different frequencies. During the measurement for the "T2-R2", the position of the receiver R2 deviated from the actual position leading to a narrow beam angle. The error for the measured and the calculated value increases in the second configuration. Doubling the distance measurements led to a decrease in the signal strength, which may have been the reason for the increase in the error.

During the measurement for the configuration of "R3-T3", due to the insufficient signal strength of the echo, it was not possible to perform reliable measurement. Hence, the configuration was changed to "T1-R2".

Config.	Wind Speed	Frequency MHz	RCS dBm^2	RCS Error	Received Power dBm	Power Error
T1-R1	24 km/hr	200	27	-3	-43	3
		235	29	-	-43	-
		605	29	-1	-58	1
T2-R2	6-22 km/hr	235	24	6	-59	6
		605	28	-2	-69	2
T1-R2	10 km/hr	50	11	-19	-58	11
		60	12	-18	-58	18
		280	33	3	-47	-3

Table 5.3: Measurement results

5.5. Conclusion

Based on the results on the Lagerweg L100-Lelystad NL WT, It can be seen that for frequency range 200-280 MHZ the results were fairly good. The influence of the near-field effect maybe have lead to some underestimation of the measurement results. The applied method is not suitable for distances greater than 2km due to insufficient signal strength.

6 Simulations and Analysis

In the previous chapters, the background of the model, the state-of-art, and the step by step further development of the wind turbine scattering model was addressed. In this chapter, the results are simulated in MATLAB using the previously presented mathematical derivations and extensions. Some general results are compared with the pre-existing model to highlight the basic working of the model. The results are further compared and validated using data from a real-time measurement carried out by the Agentschap Telecom. This is an important step which attributes to the accuracy and reliability of the proposed model.

The mono-static scattering and bi-static scattering models for the EM model were derived and explained in Chapter 4. As mentioned earlier, the frequency of interest lies in the VHF and UHF bands. Keeping this in mind, the model is simulated for three primary frequencies, *i.e.*, 50 MHz, 280 MHz and 600 MHz. It should be noted that the analysis is mostly done using vertical polarization. The measurement of the theoretical model is done for a constant aspect angle (θ). To maintain the uniformity of the results, the specifications of the Lagerwey wind turbine are used for the simulations of the results of the wind turbines (WT) response. The wind turbine structure (WTS) parameters used for results simulation are tabulated in Table 6.1.

Parameter	Value
Length of the blades	57.3 m
Nominal Speed	12.6 rpm
Blades cone angle	3.5°
Hub height	91m
Number of blades	3
Tower radius	2.7 m
Length of the nacelle	12.7 m
Dielectric Constant (Steel)	1

Table 6.1: Different parameters of WTs used in the proposed model

Parameter	Value
Frequency	50, 28, and 600 MHZ
Bandwidth	28 MHz
PRF	1kHz
NFFT points	256/1024
Window function	Hamming Window
Time overlay	99%

Table 6.2: Different signal parameters of WTs used in the proposed model

To illustrate the results obtained for the proposed model, spectrograms (**in dB**) (Section 2.4) is used in this chapter. The short-time Fourier transform (STFT) of the results were simulated for a Hamming window for 256 samples with 99% overlapping for all the cases analyzed in the following sections. Besides, the results of applying other window functions, such as Blackman window function. A summary of all the signal parameter used in the result simulation is tabulated in Table 6.2.

6.1. Mono-Static Scattering Model

The micro-Doppler pattern of the developed model for WT using a stepped frequency waveform with PRF 1kHz and a bandwidth of 28MHz. The simulation for mono-static scattering case was carried out at an aspect angle θ equal to 60°. For all the frequencies, the results are shown in Fig. 6.2 - 6.6 for all polarizations. It can be seen that the fields corresponding to each blade have forward and backward field in consecutive turns. For all the simulation, the blades are rotating at 15 rpm with a blade length of 57.3 m and with PRF of 1 kHz. In the mono-static scattering model, it is assumed that there is no mutual coupling between the dipoles and the reflection from the ground is not taken into account.

Generally, a HAWT is made up of three blades which has an angular distance of 120° between two consecutive WTB. The orientation of the WT with this separation makes the blades flash alternating. The time between these flashes is determined from the rpm of the WT blades. The fields corresponding to each blade have forward and backward field in consecutive turns in both the sides of the zero Doppler spectrum with vertical polarization. These flashes occur when the blade is perpendicular to the RLOS. The mechanism of positive and negative Doppler is illustrated in Fig, 6.1. The position of the blades is shifted by 180° after a certain angle of rotation. Thus, the positive and negative Doppler can be seen in the spectrogram because of this mechanism.

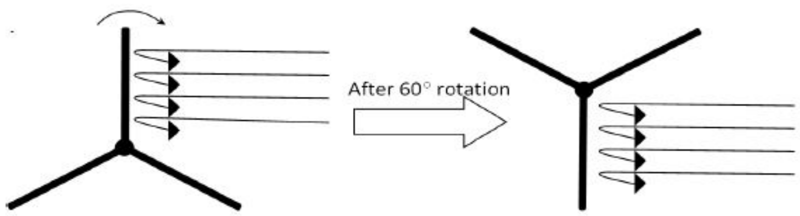

Figure 6.1: Mechanism giving rise to positive and negative for a blade rotation [4].

The trail of the path of the blades results in this sinusoidal like nature. In theory, the spectrogram has a sinusoidal distribution, and it is so far observed in the previous model and also depicted in Fig. 6.9. The halo around the tip of the blades could be due to the strong reflection from the tip of the blade. These can be filtered out using a window function. Hence, a flash occurs at different positions along the blade as a function of time.

The results of different polarization are also shown in the figure. It comes with no surprise that the cross-polarization results are the same for the mono-static scattering case. Because from the reciprocity theorem, the off-diagonal elements of the S-matrix are equal ($S_{VH} = S_{HV}$). As for the horizontal polarization, the result of zero Doppler is absent, but the reflected signal has poor strength compared to the vertical polarization. For the results of VH and HV polarization, the zero Doppler components are suppressed completely however for HH polarization, there are faint trails where zero - Doppler are present. This maybe because for VH and HV polarization, the side lobes of lead to complete zero-Doppler. For the HH polarization, it can be that the broadside lobes of the dipoles suppress the zero-Doppler. However, due to the constant rotation of blades, it may not be possible and leading to the zero-Doppler at certain ϕ.

In Fig. 6.3, the result of applying Blackman window is shown. The thin peaks at the end of the tips are filtered out by the window function. Though it is clear that Blackman window has better side lobes suppression, Hamming window was chosen for the result simulation of the proposed model. Applying window function, along with the side lobes suppression, increases the size of the main lobes and this impacts the range resolution by decreasing it. The result for frequencies 280 MHz and 50 MHz are shown in Fig. 6.4 and Fig. 6.6 along with the windowing result in Fig. 6.5 and Fig. 6.7, respectively.

The absence of zero Doppler in the HV and VH polarization is very prominent in the spectrogram results for f = 50MHz Fig. 6.6b and Fig. 6.6b.

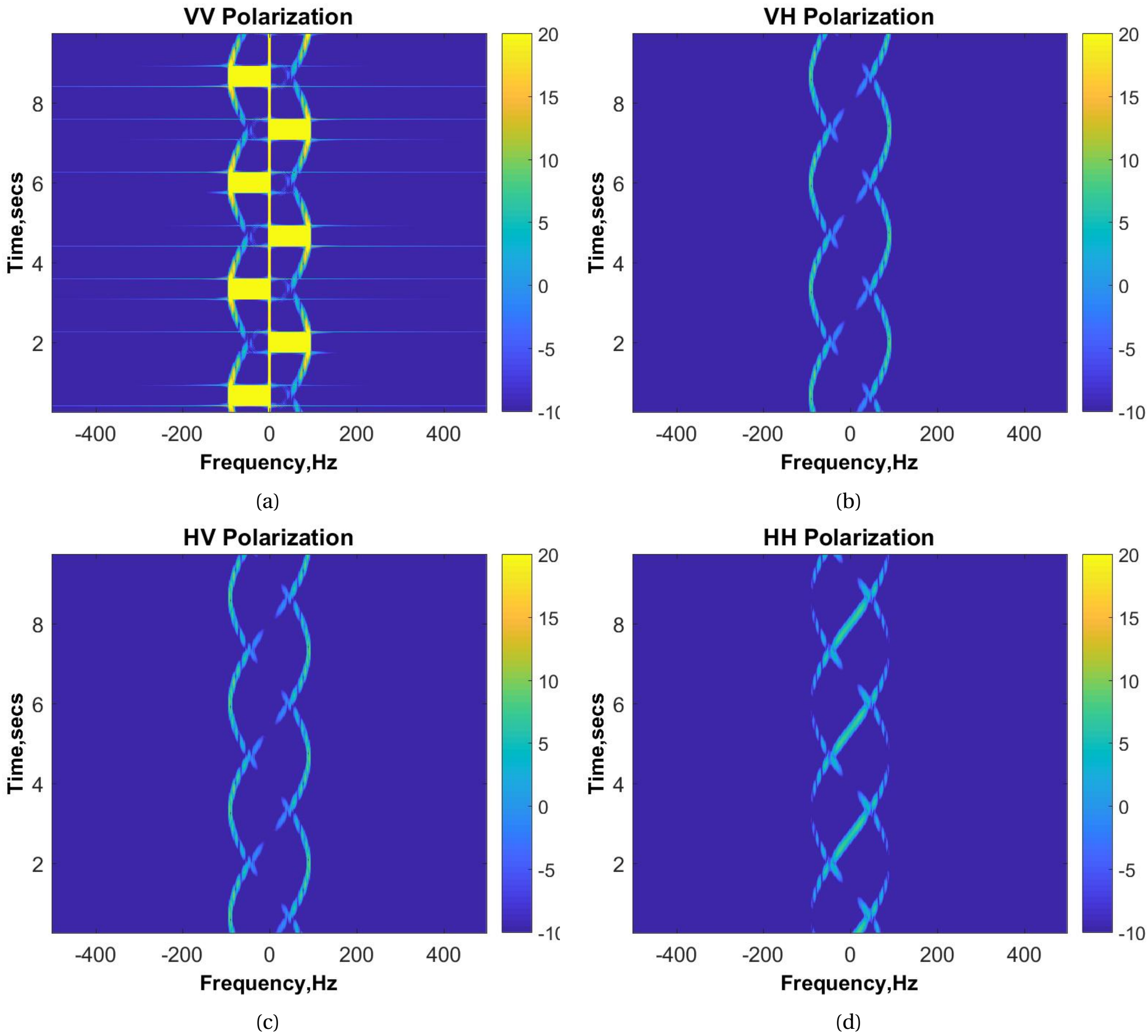

Figure 6.2: Spectrograms showing the results of mono-static scattering model for different polarization shown in each figure for the frequency 600 MHz at aspect angle $\theta = 60°$: (a) Vertical Polarization; (b) & (c) Vertical and horizontal cross polarization; and (d) Horizontal Polarization. The dynamic range has been reduced to accommodate the low strength of the VH, HV, and HH polarization.

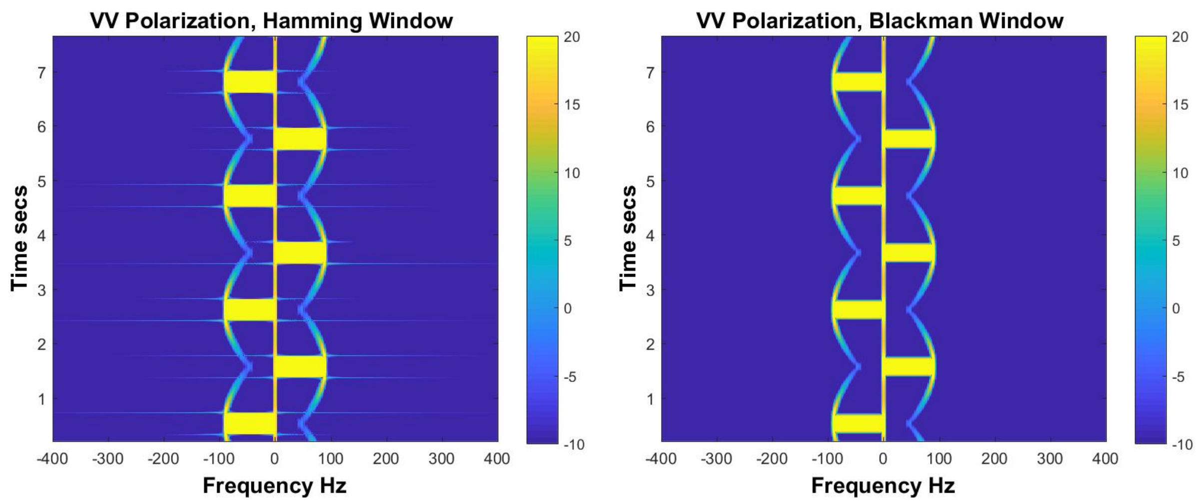

Figure 6.3: Spectrograms showing the results of mono-static scattering model for Hamming and Blackman window function for the frequency 600 MHz at aspect angle $\theta = 60°$.

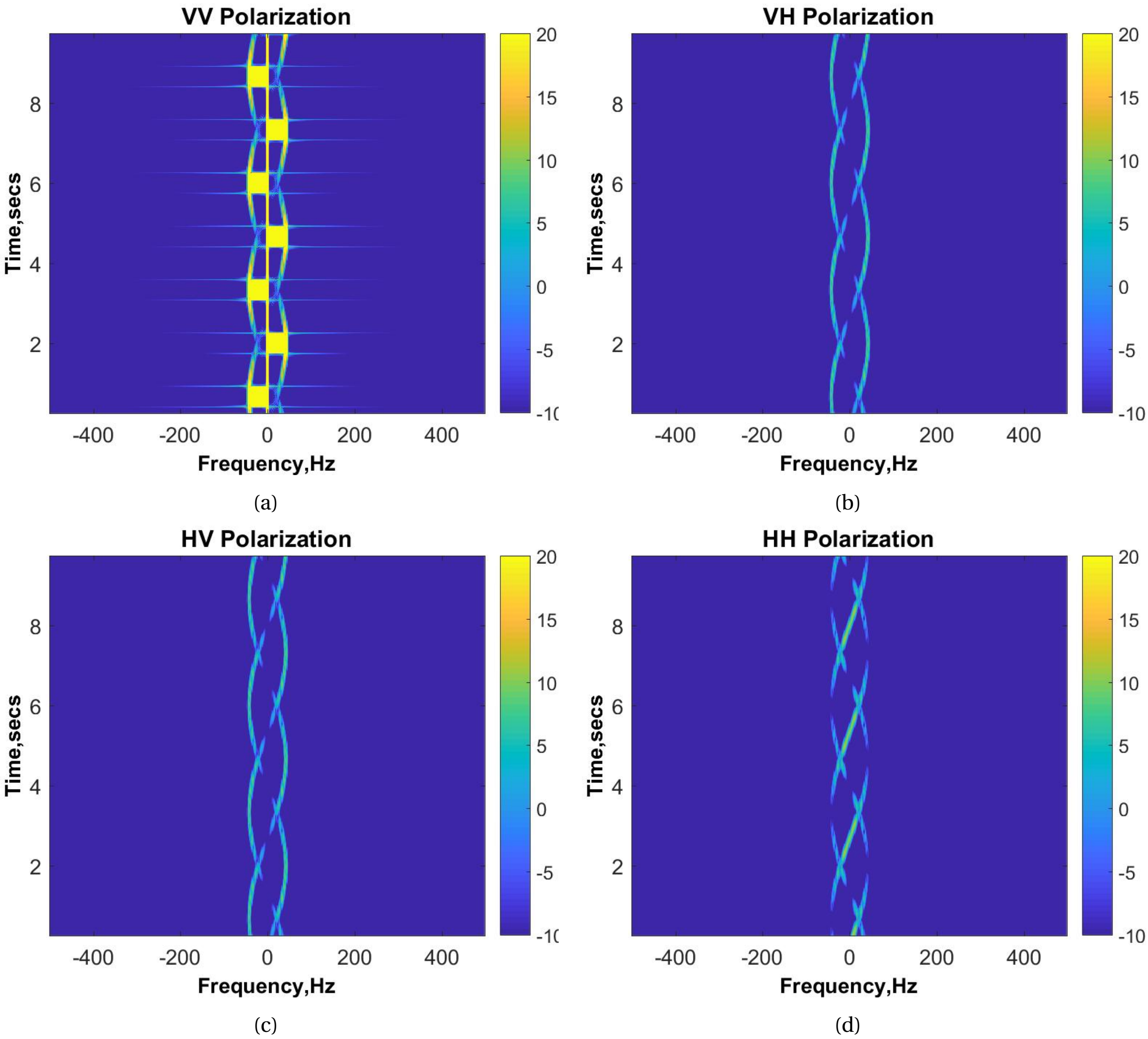

Figure 6.4: Spectrograms showing the results of mono-static scattering model for different polarization for the frequency 280 MHz at aspect angle $\theta = 60°$: (a) Vertical Polarization; (b) & (c) Vertical and horizontal cross polarization; and (d) Horizontal Polarization. The dynamic range has been reduced to accommodate the low strength of the VH, HV, and HH polarization.

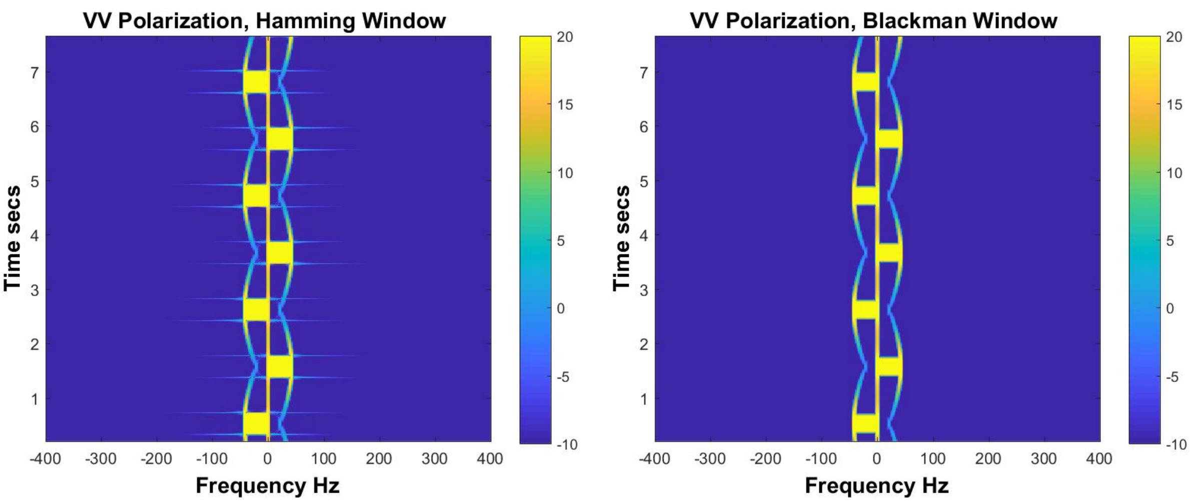

Figure 6.5: Spectrograms showing the results of mono-static scattering model for Hamming an Blackman window function for the frequency 280 MHz at aspect angle $\theta = 60°$.

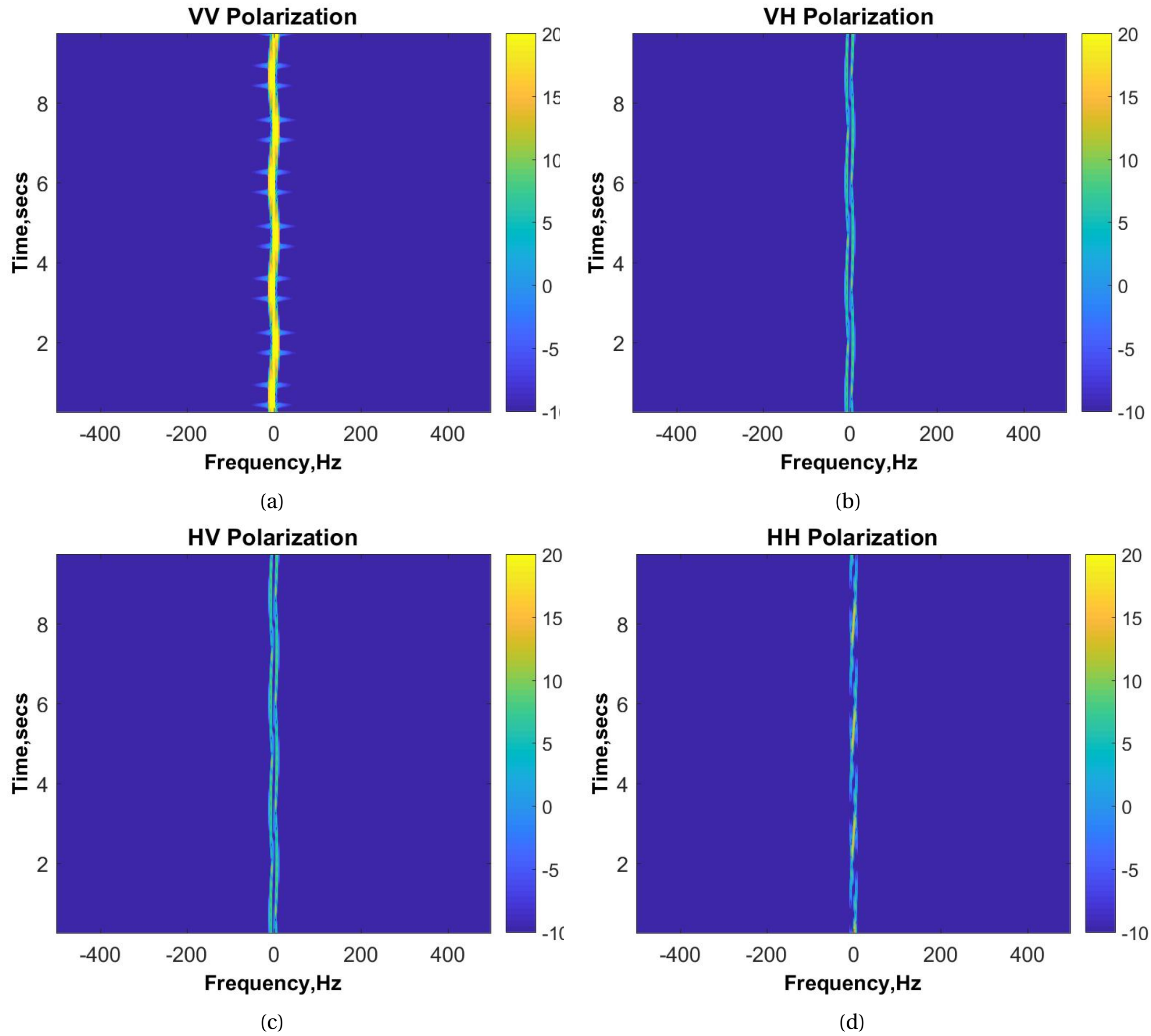

(a) (b) (c) (d)

Figure 6.6: Spectrograms showing the results of mono-static scattering model for different polarization for the frequency 50 MHz at aspect angle $\theta = 60°$: (a) Vertical Polarization; (b) & (c) Vertical and horizontal cross polarization; and (d) Horizontal Polarization.

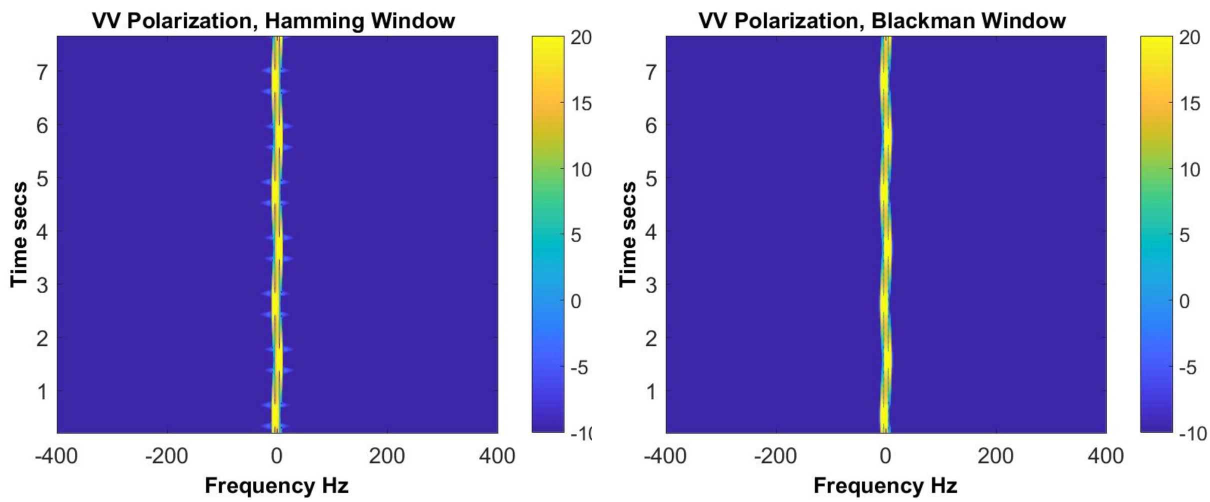

Figure 6.7: Spectrograms showing the results of mono-static scattering model for Hamming and Blackman window function for the frequency 600 MHz at aspect angle $\theta = 60°$.

Because of the small magnitude of the frequency, the Doppler shift and the zero-Doppler is not distinguishable in the Fig. 6.6a.

6.2. Bi-Static Scattering Model

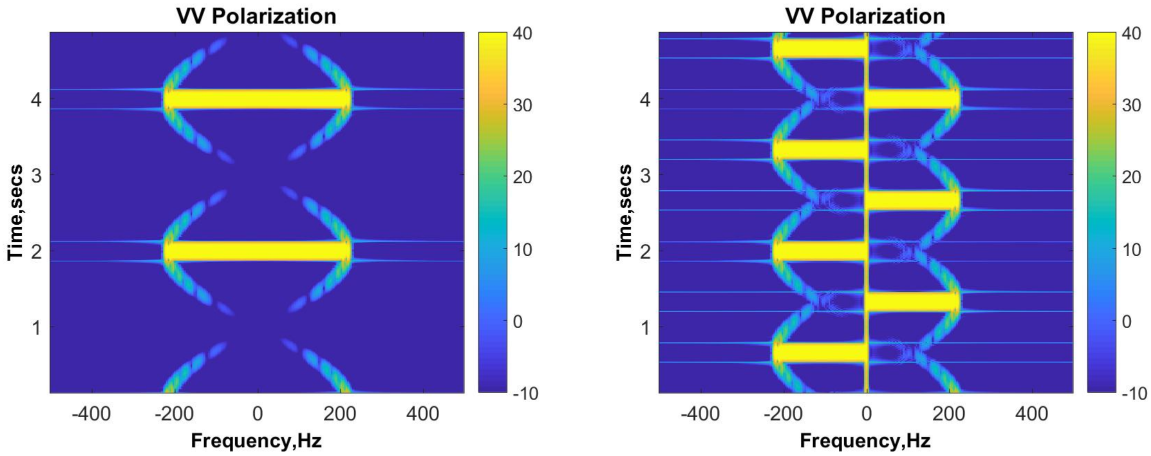

(a) (b)

Figure 6.8: Micro-Doppler signature of the results of model and literature: (a) Spectrogram with even number of blades; and (b) Spectrogram of odd number of blades.

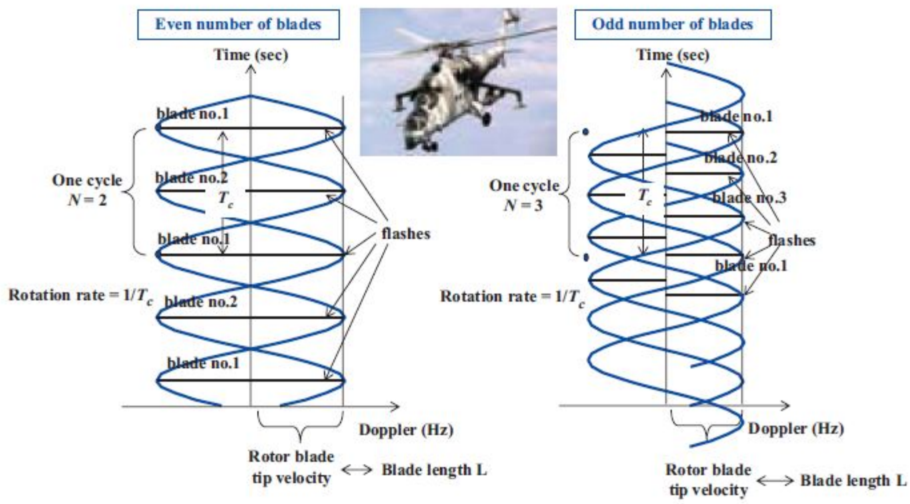

Figure 6.9: General micro-Doppler signature of even and odd numbers of blades [7].

The micro-Doppler signature of the WT with an even and an odd number of blades are depicted in Fig. 6.9. It is evident that the pattern from the even and odd number of blades are different, which is also apparent from Fig. 6.15a and 6.15b. The even number of blades will induce a symmetry around the mean Doppler frequency, whereas the odd number blades will result in an asymmetric pattern.

The spectrograms of the bi-static scattering model for different polarization are presented in Fig. 6.10 for frequency f_m = 600 MHz. Unlike the mono-static scattering case, the off-diagonal matrix need not be same. This can be seen from the Fig. 6.10. The VH polarization results have stronger signal strength compared to the HV polarization result. As for the HH polarization result, there seems to be a minimum Doppler shift at two other frequencies. This may be due to the rotation of the blades and the aspect angles, the Doppler suppression seems to have 'shifted'.

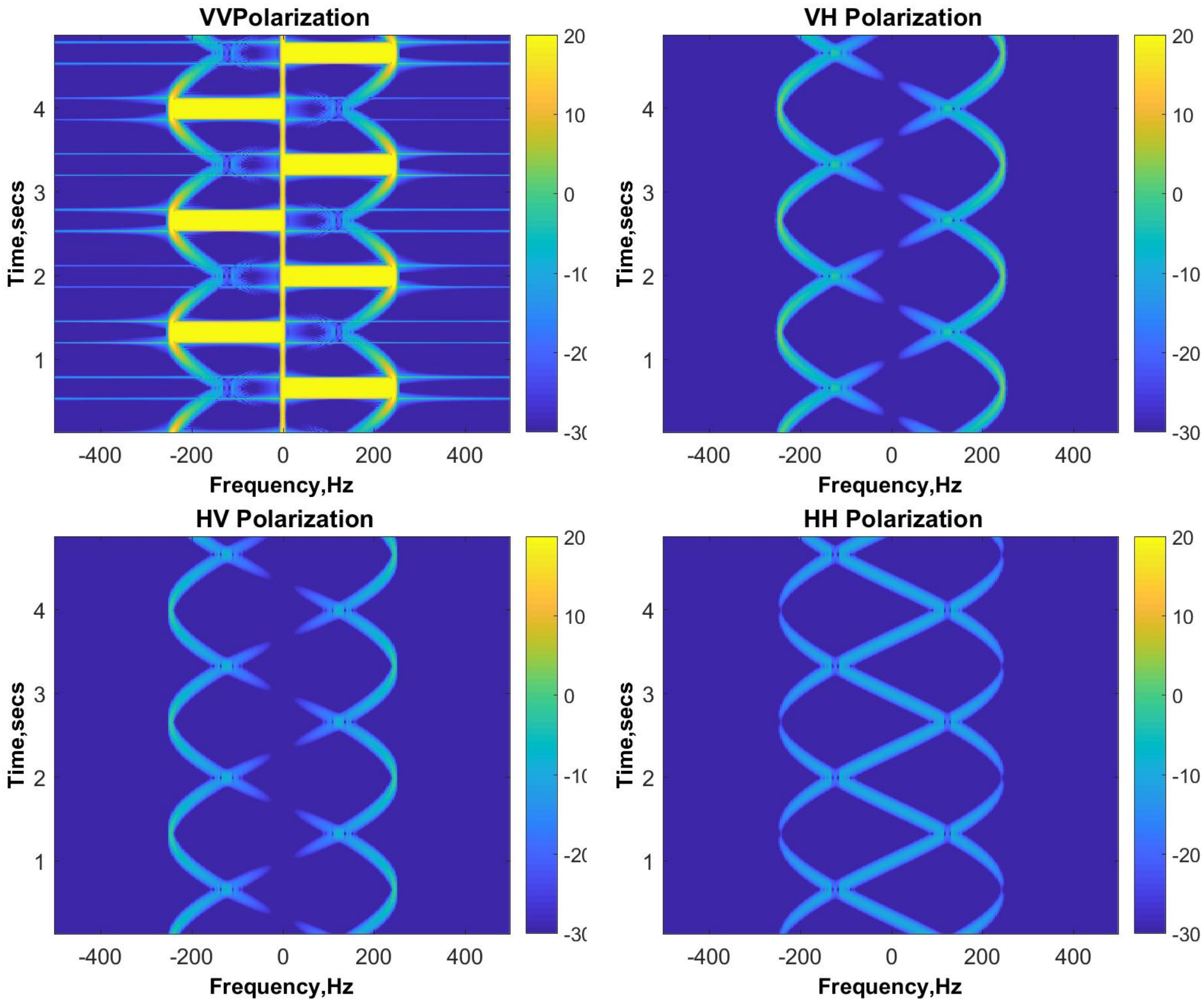

Figure 6.10: Spectrograms showing the results of bi-static scattering model for different polarization for the frequency 600 MHz at $\theta_i = 30°$ and $\theta_s = 60°$: (a) Vertical Polarization; (b) & (c) Vertical and horizontal cross-polarization; and (d) Horizontal Polarization.

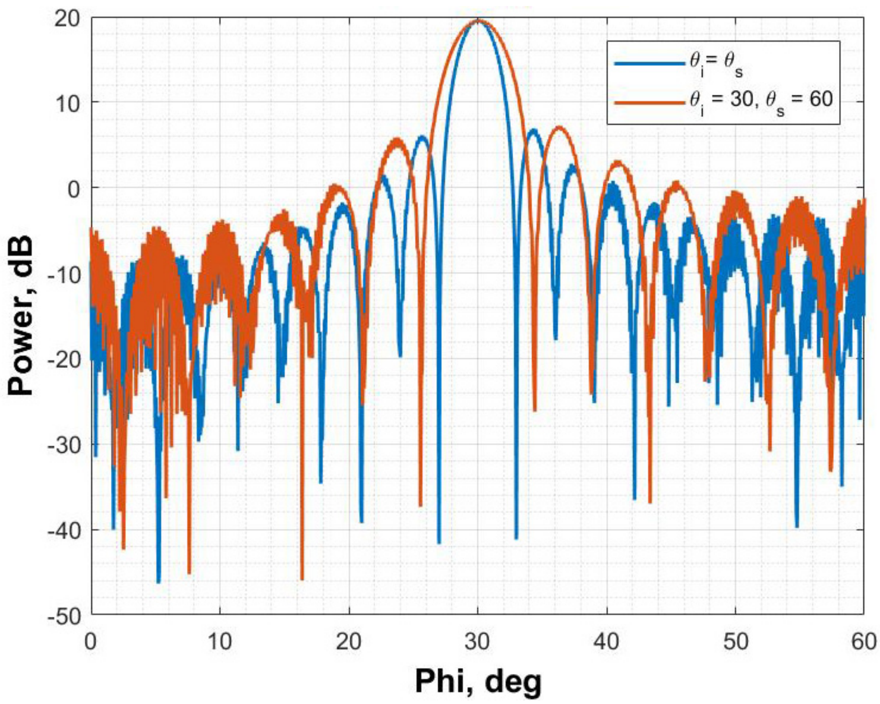

Figure 6.11: Comparison of the mono-static scattering model and the bi-static scattering model for f_m = 600 MHz at 12.6 rpm for **VV Polarization**.

To study the results of the bi-static scattering model, different cases were implemented to observe how the proposed model perform and analyze. The four different cases for the bi-static study are tabulated below in Table 6.3.

Case	1a	1b	1c	1d
Incident angle, θ_i	0°	30°	45°	45°
Scattered angle,θ_s	0°	60°	315°	135°

Table 6.3: Different cases to study the bi-static scattering model.

For Case 1a, the results are similar to the case of a mono-static scattering case. The spectrum of case1a with case 1b is plotted in 6.11. In general, the bi-static coverage is lesser than the mono-static coverage; the amplitude remains the same [51]. This can be seen from Fig. 6.11 that the bi-static scattering has stronger distribution (more coverage) than the bi-static case. For case 1c and 1d, the results are expected to have opposite Doppler but, in the latter case, since θ_i and θ_s are out of phase, destructive interference may have occurred resulting in the scattering canceling each other out (Fig. 6.12d), leading to a very strong zero-Doppler.

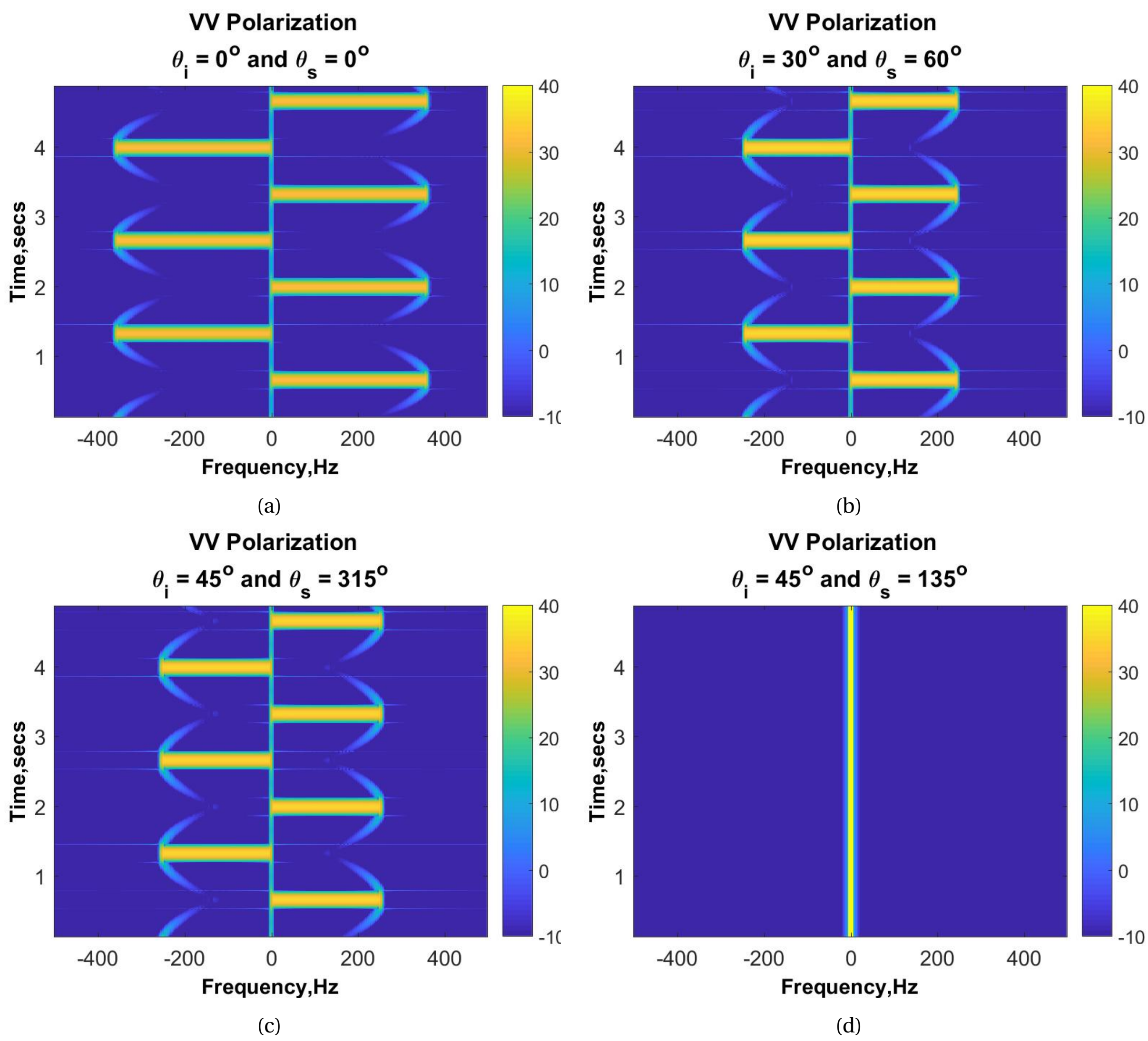

Figure 6.12: Spectrograms for different cases of θ_i and θ_s tabulated in Table 6.3 for the frequency 600 MHz: (a) Case 1a; (b) Case 1b; (c) Case 1c; and (d) Case 1d

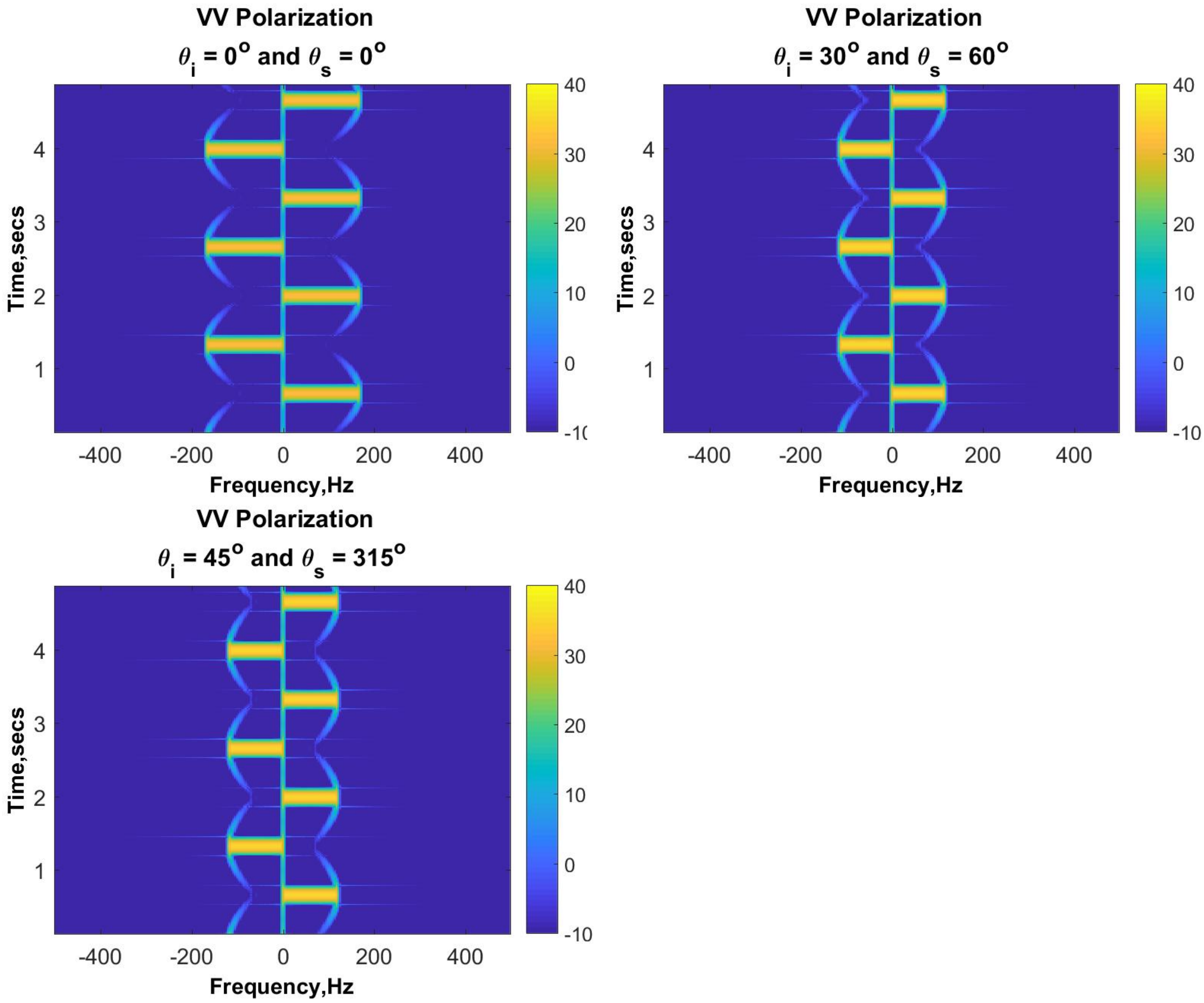

Figure 6.13: Spectrograms for different cases of θ_i and θ_s tabulated in Table 6.3 for the frequency 280 MHz: (a) Case 1a; (b) Case 1b; and (c) Case 1c.

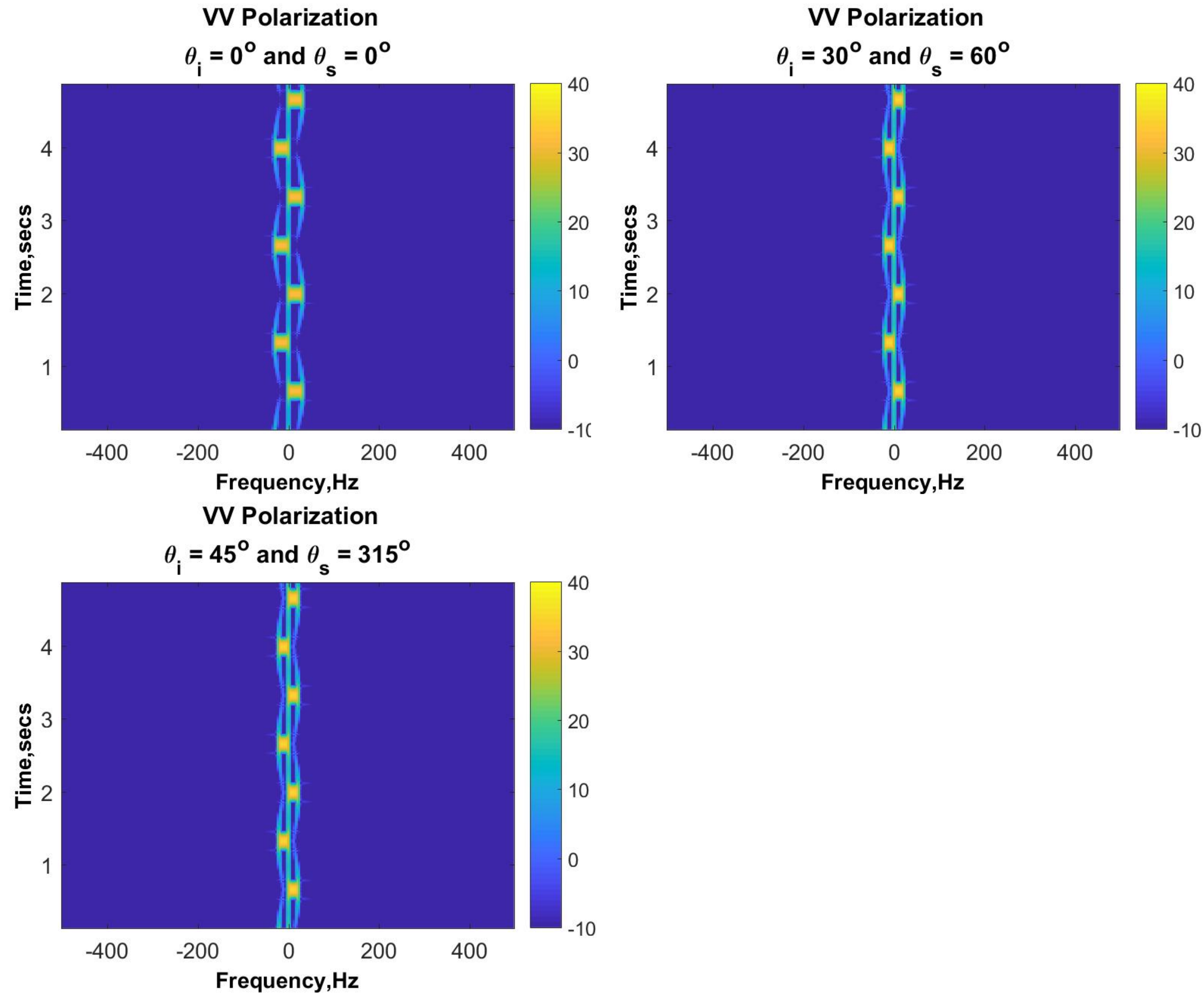

Figure 6.14: Spectrograms for different cases of θ_i and θ_s tabulated in Table 6.3 for the frequency 50 MHz: (a) Case 1a; (b) Case 1b; and (c) Case 1c.

6.3. Comparison of Simulations with Experiment

In Chapter 5, the experimental set up to determine the reflecting surface of a WT was explained and the results were discussed [13]. The results obtained are validated with the numerical results from the proposed model. The signal strength for the cases for the present model is then plotted to analyze the results.

In the report [13], since numerical results were provided, the data validation can only be done using relative error and ratio. From the radar range equation 2.2,

$$P_r = \frac{P_t G_t G_r \lambda^2 \sigma}{(4\pi)^3 R^4} \tag{6.1}$$

$$\sigma = \frac{P_r R^4}{a(\lambda)} \tag{6.2}$$

where $a(\lambda)$ is a constant parameter used in the experiment. With the theoretical model, only Σ is known to us. Thus, using the ratio

$$\frac{P_r(f_1)}{P_r(f_2)} = \frac{\lambda_2^2 \sigma(f_1)}{\lambda_1^2 \sigma(f_2)} \tag{6.3}$$

The difference in the signal strength can be evaluated. Using the expression from 6.3, the error calculation can be done. The results obtained are then tabulated in Table 6.4.

Configuration	Frequency	Signal Strength		Difference		Error(dB)
		Model	Measured	Model	Measured	
T1-R1	200 MHz	15.88	40			
	600 MHz	25.37	57	19.08	17	2.8
T2-R2	235 MHz	8.02	53			
	605 MHZ	15.94	67	16.06	14	2.06
T1-R2	60 MHz	35.32	39			
	280 MHz	48.62	50	26.6	11	15.6

Table 6.4: Comparison of numerical results of the EM model and the results from the experiment carried out by the Agentschap Telecom by comparing the signal strength of the radar return for bi-static scattering angle of $\theta_{bistatic} = 90°$ ($\theta_i = 30°$ & $\theta_s = 60°$.

$$\frac{P_{200}}{P_{600}} = 57 - 40 = 17\,\text{dB}$$

$$\frac{\lambda_2^2\sigma(f_1)}{\lambda_1^2\sigma(f_2)} = \left(\frac{235}{600}\right)^2 + (9.5) = 19.08\,\text{dB}$$

$$\frac{P_{235}}{P_{605}} = 67 - 53 = 24\,\text{dB}$$

$$\frac{\lambda_2^2\sigma(f_1)}{\lambda_1^2\sigma(f_2)} = \left(\frac{235}{605}\right)^2 + (7.92) = 16.06\,\text{dB}$$

$$\frac{P_{60}}{P_{280}} = -39 + 50 = 11\,\text{dB}$$

$$\frac{\lambda_2^2\sigma(f_1)}{\lambda_1^2\sigma(f_2)} = \left(\frac{60}{235}\right)^2 + (13.30) = 26.6\,\text{dB}$$

The error for the configuration of T1-R2 very high. This was also the case during the measurement carried out by the Agentschap Telecom. It was due to the insufficient signal strength and limitations due to the larger distance. The measurements model was not suitable for measurements carried out for a distance greater than 2 KM [13]. Thus, the large error in the calculation.

The data received from the device setup is analyzed in the VNA. Fig.6.15, the image of the vector analyzer and the results simulated in MATLAB using the model are shown for the frequency of $f_m = 60$ MHz.

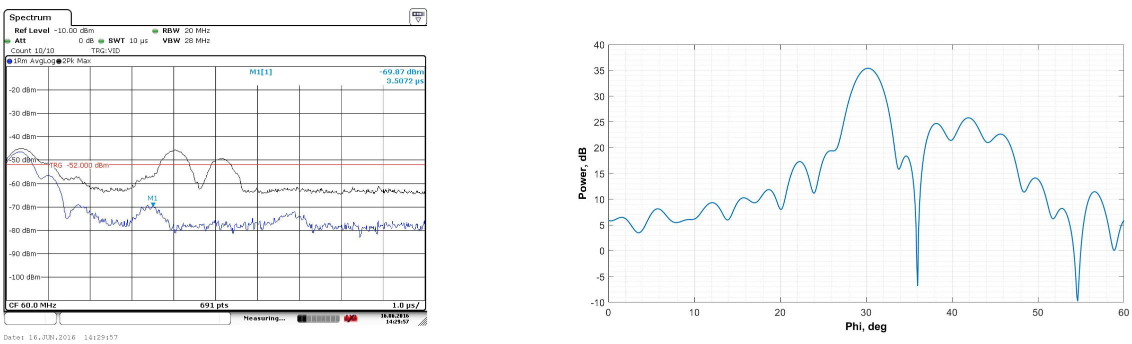

(a) (b)

Figure 6.15: (a) Image of the signal in VNA in time domain [13]; (b) Figure simulated in MATLAB using the proposed model.

6.4. WT Range Profile

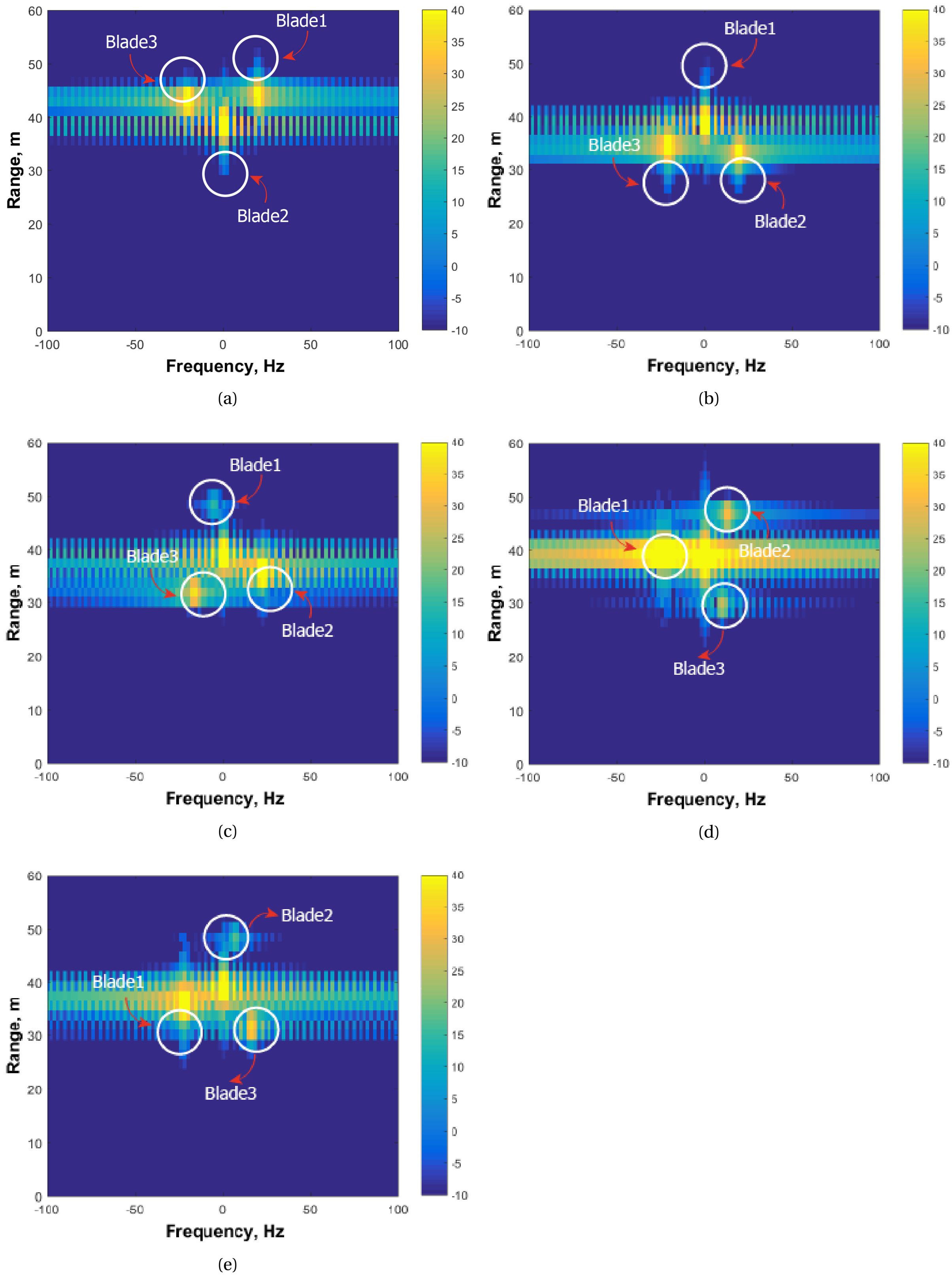

Figure 6.16: Range profile of mono-static scattering model for different stepped frequencies for bandwidth B = 28 MHz and f_m = 600 MHz for an aspect angle of 60°. The motion of the blades is in counter clockwise direction. Thus, the profile order goes like (a)-(b)-(c)-(d)-(e). The stationary point at the center is the rotation center of the wind turbine.

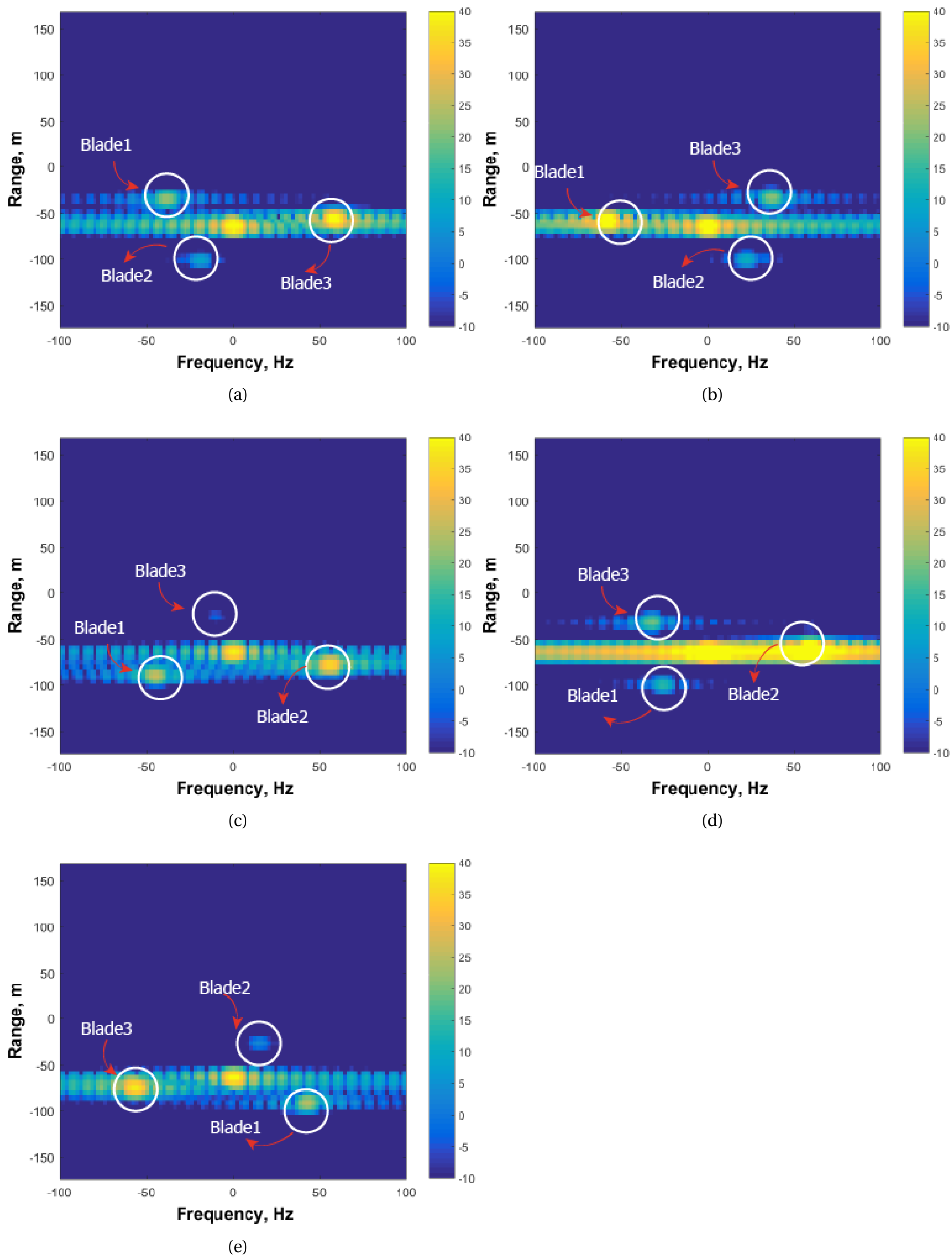

Figure 6.17: Range profile for bi-static scattering model steps for bandwidth B = 28 MHz and f_m = 600 MHz for θ_i = 30° and θ_s = 60°. The motion of the blades is presented in counter clockwise direction. Thus, the profile order goes like (a)-(b)-(c)-(d)-(e). The rotation point of the wind turbine is the stationary point at the center.

In this section, the range profile of the wind turbine blades rotation is shown. In Fig. 6.16, the range profile shows the rotation of the three blades in a counter-clockwise direction. As mentioned earlier, the flashes in the spectrogram were a result of the blades in orthogonal position. It can also be seen in the Fig. 6.16d. Similarly, the flashes can be seen for the bi-static case in Fig. 6.17d.

The center of the rotation of the wind turbine has strong zero-Doppler component. However, there is certain shift in the range in the range profile as seen in the figures. One of the reason maybe the scaling error after the FFT. Another possible reason, maybe due to range aliasing. From Chapter 2, the range resolution (2.3) and the unambiguous range (2.6) are related as

$$R_u = \frac{c}{\Delta f} = N\Delta R \tag{6.4}$$

This trade-off may have led to the range aliasing since N ismd large to attain fine range resolution .

6.5. Contribution of Mast

In the previous sections, the radar micro-Doppler signatures and the range profiles of the WTBs were studied and analyzed using spectrogram. In addition to the motion of the blades, the other stationary parts of the WT also has an impact the scattering properties of the WTSs. Thus, to completely understand the scattering of the WT, the mast of the wind turbine has been implemented in the model design. The tower/mast of a WT is modeled as a dielectric electric cylinder of radius a and height L_{hub}.

After all the results for the mono-static and bi-static scattering have been analyzed, it is important to compare the data for the three different cases, mono-static scattering, bi-static scattering, and influence of mast on the scattering model. In Fig. 6.18, the signal strength of the three different cases are illustrated. The signal strength of the mono-static scattering model is highest, and the bi-static scattering model is the minimum. In similar comparison with pseudo mono-static and bi-static scattering case in Fig. 6.11.

Since mono-static scattering case has stronger distribution, it is apparent that it would have more signal return. The influence of mast resulting is in greater signal return for bi-static scattering case is similar to the discussion in Chapter 3 [51].

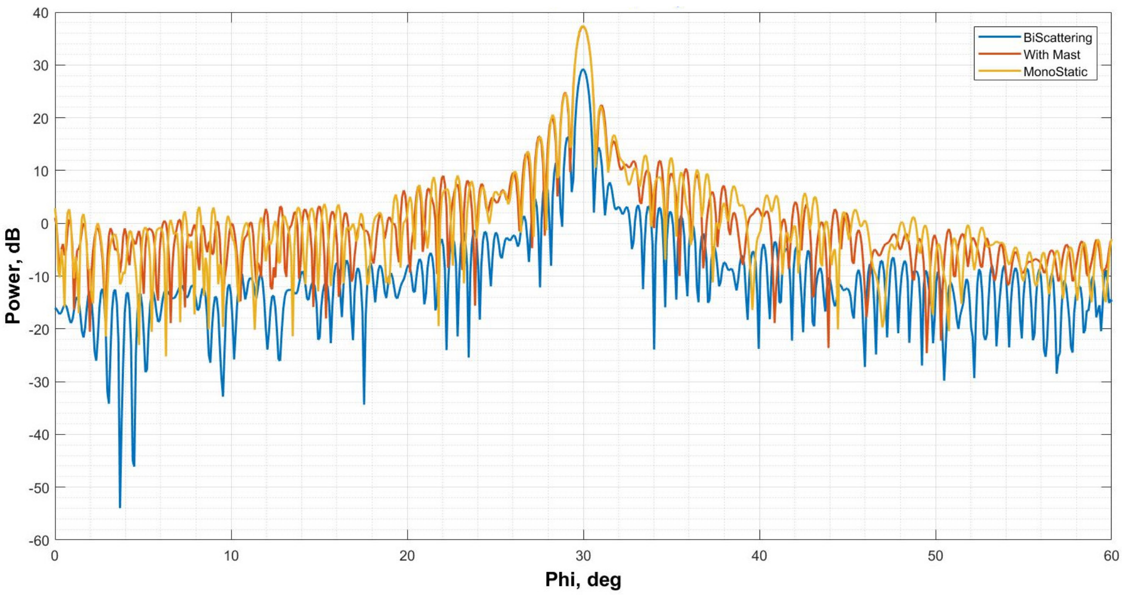

Figure 6.18: Comparison of the signal return for the three cases with **VV Polarization** for f_m = 600 MHz at θ = 60° for mono-static scattering case and θ_i = 30°, θ_s = 60°

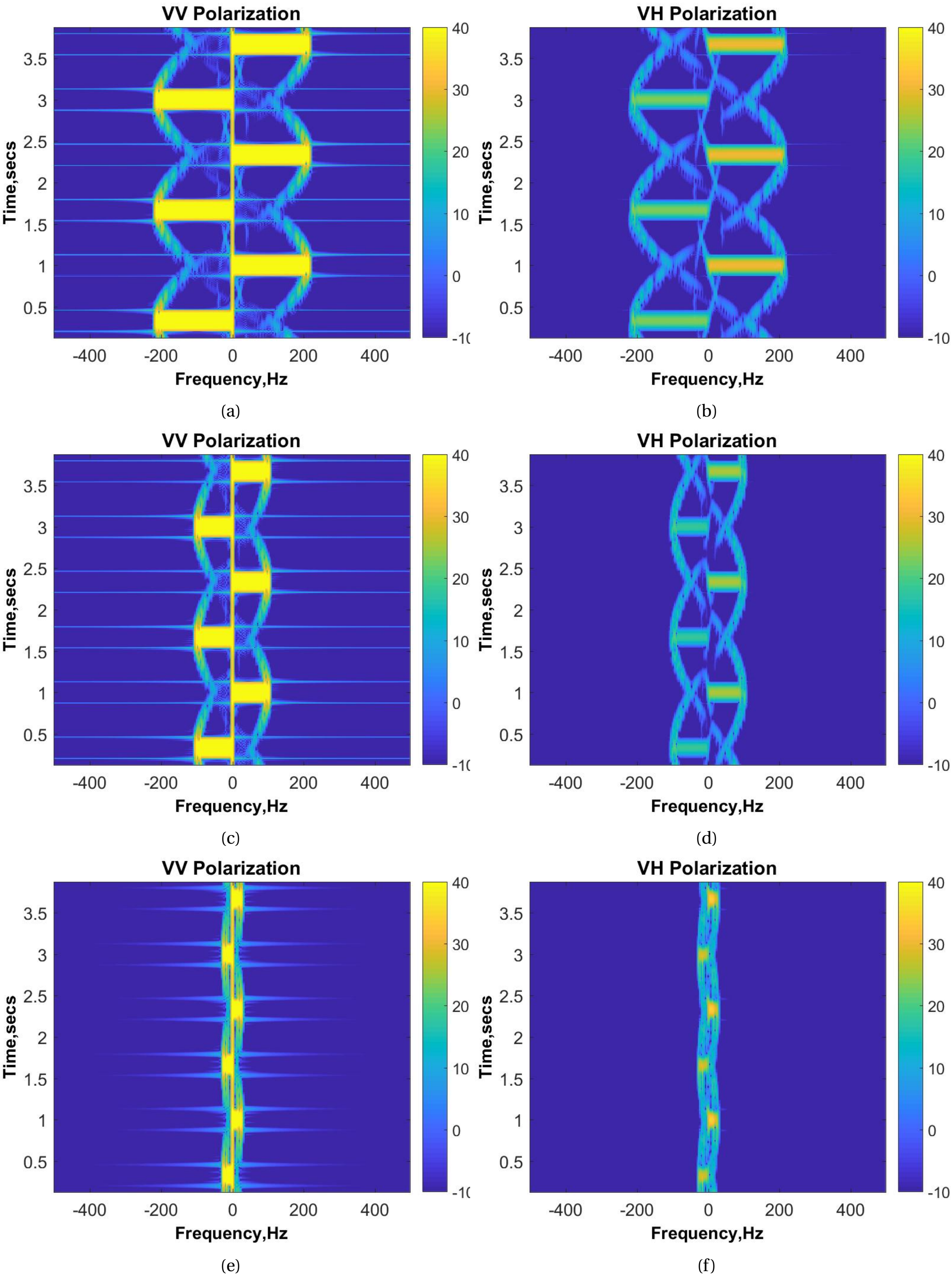

Figure 6.19: Spectrogram of the VV and VH polarization results with the influence of mast for frequencies at $\theta_{\mathbf{i}} = 30°$, $\theta_s = 30°$ for a bandwidth of 28MHz: (a)&(b) 600 MHz; (c)&(d) 280 MHz; and (e)&(f) 50 MHz.

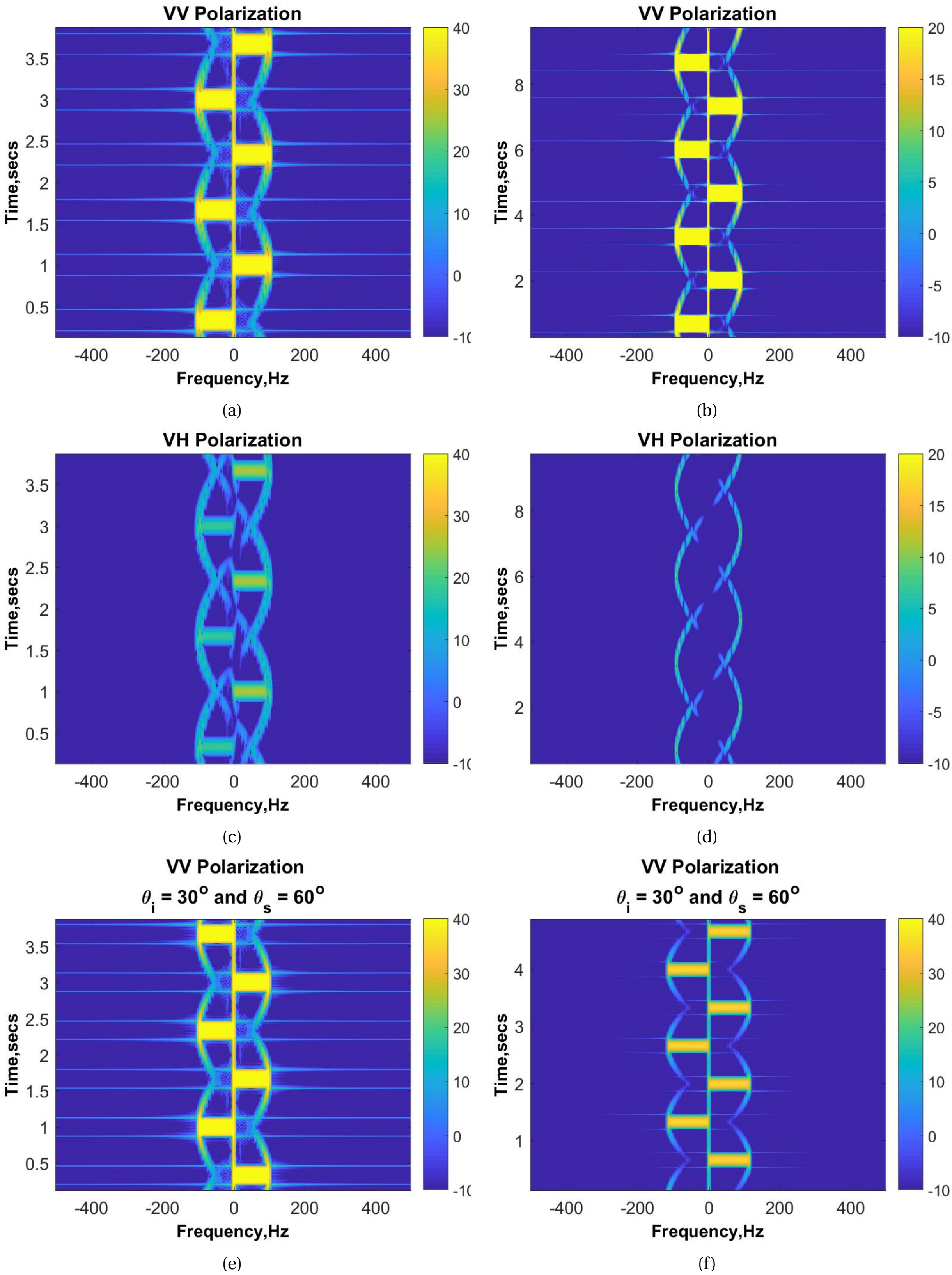

Figure 6.20: Comparison of the resulting spectrogram of the influence of mast with the mono-static scattering case and bi-static scattering case for different polarization at f_m = 280 MHz: (a)&(b) VV Polarization for mono-static scattering case; (c) & (d) VH Polarization for mono-static scattering case; and (e) & (f) VV Polarization for bi-static scattering case.

The resulting spectrogram depicting the influence of mast for the proposed model is shown in Fig. 6.19. After the addition of the mast in the model design, the resulting model was expected to have a stronger zero-Doppler return, as seen in Fig. 3.12 in Chapter 3, as compared to the previous results. The results are somewhat close to expected with but with lower zero-Doppler strength.

Another observation is that there is a sinusoidal trail around the Zero-Doppler. It can be noted that the trail somewhat looks similar to the case of horizontal polarization in Fig. **??**. This could be due to the reflection of the signal from the mast to the blades; the mast acting as a reflecting medium for the blades in proximity. The difference in the signal strength of the bi-static and mast contribution should be taken into account. The importance of this observation has been explained in section 3.3.

Another very interesting observation in the case of the mast is the resulting horizontal polarization. The horizontal polarization seems to be very similar to the vertical polarization, except the signal strength is comparatively lower in the former case. This could be because the axis of the mast is always perpendicular to the axis of the polarization. So, regardless of the orientation of the plane, the mast will always influence the horizontal polarization.

6.6. Conclusion

The results for the mono-static scattering and bi-static scattering were discussed. The mono-scattering case was implemented for one aspect angle whereas the bi-static scattering model was implemented for four different cases. Any additional simulation was implemented using VV-Polarization; such as study of windowing function and different bi-static scattering cases, and range profile.

It was found that the zero-Doppler component of the WT has stronger presence in VV Polarization than the rest of the polarization whereas the VH and HV polarization have complete suppression of zero-Doppler. The flashes due to the blades rotation were more pronounced in the vertical polarization component (VV). The importance of the used of very high (VH) and ultra high (UH) frequency bands were validated using the data provided by the Agentschap Telecom. It was seen that 280 MHz has the best performance having low error for the proposed model.

Another observation was the shift in the range of the range profile, which may be a result of range aliasing phenomena. The model was further extended for mast contribution in the WT scattering. There were sin-like trails around the zero-Doppler component, which are assumed to be due to the interaction of the tower and the wind turbine blades. Comparison of the signal strength for the mono-static and bi-static scattering with the contribution of the mast were carried out which were similar to the results in literature.

7 Conclusion and Recommendations

7.1. Conclusion

In this thesis, a simplified electromagnetic model for scattering on wind turbines (WT) blades and mast was developed using a thin wire approximation. The model was designed and developed to study the influence of wind turbines on the scattering of the radar signals for VH and UH frequency bands. Model for both mono-static scattering and bi-static scattering were designed and validated. The model was further enhanced for practical application by including a full 3-D polarimetry. To attain fine the range resolution without a wide-bandwidth, pulse compression using stepped frequency waveform was used for the signal model.

The model design of the scattering of the radar returns from the wind turbine blades was extended to include the contribution of the tower on the scattering properties of WT. These features of the model were implemented for bi-static scattering case. The shortcoming of the computational effort in simulating complex algorithm is reasonably addressed in the model using it simplified model.

The electromagnetic model result was validated using the data provided by the measurement set up done by the Agentschap Telecom. The result validated implies that even if the model is simplified, it still fulfills the objective of delivering reasonably accurate results, close to the practical results.

Therefore, as a conclusion:

- The simplified model developed using the thin wire approximation provides reliable results, and these results were validated using real measurements data. One of the aims of the model was to validate its performance in the VH and UH frequency bands. As expected the performance of the model is better especially for frequencies at 280 MHz and 600 MHz as compared to 50 MHz. The poor results of this frequency may be due to the limitation of the measurements set up.
- The zero-Doppler suppression in the horizontal polarization was a new development in the results. However, it may be a result of side lobes suppression too. The flashes of the blades were observed when they were orthogonal to the RLOS, which has been the case in previous works of literature.
- Strong reflections from the tip of the wind turbine blades (WTB) were prevalent in the spectrograms, along with the sin-like trails tracing the path of the blades. This strong reflection could be suppressed using proper window function. since it affects the range resolution, it's a trade-off between fine range resolution and side-lobes suppression.
- The model was simulated for high-resolution range profile using stepped frequency waveforms and pulse compression. The range profile clearly illustrated the motion of the wind turbine blades (WTB), but it has a unusual shit in the range. One of the explanations for the shift maybe a result of range aliasing.
- The performance of the mono-scattering model and bi-static scattering model were compared with one another. The results were similar to the general observation available in the literature.

- Lastly, the contribution of the mast in the wind turbine scattering have given some interesting results. Firstly, the zero-Doppler component was weaker than expected. In addition to that, there are presence of sinusoidal trails around the zero Doppler. It is assumed to be a result of the interaction of the blades with the tower. However, regarding the signal strength contribution, it had higher radar return compared to the bi-static scattering model.
- The results of the developed EM model can enhance the understanding and modeling of the non-stationary and micro-Doppler signatures of wind turbine clutters (WTC). The results were supported by analytical arguments. The analysis from the results will improve the further development of a more effective model to study and mitigate the impact of these clutter in the radar communication.

7.2. Recommendations and Future Work

In the further extension to this model, the blades can be designed taking the mutual coupling into consideration. Also, to study the influence of multi-path in the wind turbine scattering would be another improvement. Another extension can be the influence of the variation in the blades rotation due to surrounding impacts.

Acronyms

EM Electromagnetic. xiii, 2, 8, 11, 12, 15, 23–26, 28, 29, 37, 47, 56

EMI Electromagnetic Interference. v, 1, 16

FDTD finite-difference time-domain. 15

FEM finite element method. 15

FFT Fast Fourier Transform. ix, 1, 2, 9, 10, 13, 22, 32, 50

GMAP Gaussian Model Adaptive Processing. 16

GO geometrical optics. 15

GTD geometric theory of edge diffraction. 16

HAWT horizontal-axis wind turbines. 25, 38

HF High Frequency. 22, 26

LFM linear frequency modulated. 23

LOS line of sight. 6, 34

LR Laboratory radar. 16

MoM method of moment. 15, 22, 26

PO physical optics. 15, 16, 20, 26

PRF Pulse Repetition Frequency. 6, 23, 32, 37, 38

PRF Pulse Repetition Interval. 6

PSD Power Spectral Density. ix, 15, 16

RCS radar cross section. 5, 6, 16, 20, 21, 24, 26, 29, 33

RLOS radar line of sight. 8, 17, 18, 23, 25, 27, 38, 55

STFT short-time Fourier transform. vii, ix, 2, 3, 9, 10, 13, 37

UH ultra high. v, 2, 3, 53, 55

UHF ultra high frequency. 16, 26, 37

VH very high. v, 2, 3, 53, 55

VHF very high frequency. 16, 26, 37

VNA Vector Network Analyzer. x, 16, 47

WT wind turbines. v, vii–x, xiii, 1–3, 8, 11, 15, 16, 19–29, 32, 34, 36–38, 42, 46, 48–50, 53, 55

WTB wind turbine blades. v, x, 1, 2, 9, 11, 18, 25–28, 38, 50, 55

WTC wind turbine clutters. v, ix, 1, 15, 16, 19, 23–25, 56

WTM wind turbine model. ix, 16

WTS wind turbine structure. v, 1, 2, 16, 26, 29, 34, 37, 50

Bibliography

[1] Zunhua Guo and Shaohong Li. One-dimensional frequency-domain features for aircraft recognition from radar range profiles. *IEEE Transactions on Aerospace and Electronic Systems*, 46(4):1880–1892, 2010.

[2] William Arthur Sethares. *Rhythm and transforms*. Springer Science & Business Media, 2007.

[3] Jiemin Hu, Weidong Jiang, Yaowen Fu, and Jing Ning. A novel approach to synthesize the range profile via predesigned stepped-frequency waveforms. In *Computer Engineering and Technology (ICCET), 2010 2nd International Conference on*, volume 5, pages V5–363. IEEE, 2010.

[4] Victor C Chen. *The micro-Doppler effect in radar*. Artech House, 2011.

[5] Aale Naqvi, Nick Whitelonis, and Hao Ling. Doppler features from wind turbine scattering in the presence of ground. In *Antennas and Propagation Society International Symposium (APSURSI), 2012 IEEE*, pages 1–2. IEEE, 2012.

[6] Yan Zhang, Andrew Huston, Robert D Palmer, Roy Albertson, Fanxing Kong, and Shang Wang. Using scaled models for wind turbine em scattering characterization: techniques and experiments. *IEEE transactions on instrumentation and measurement*, 60(4):1298–1306, 2011.

[7] Victor C Chen, Fayin Li, S-S Ho, and Harry Wechsler. Micro-doppler effect in radar: phenomenon, model, and simulation study. *IEEE Transactions on Aerospace and electronic systems*, 42(1):2–21, 2006.

[8] Calvin C Teague and Donald E Barrick. Estimation of wind turbine radar signature at 13.5 mhz. In *Oceans, 2012*, pages 1–4. IEEE, 2012.

[9] I Angulo, D De La Vega, O Rodríguez, O Grande, D Guerra, and P Angueira. Analysis of the mast contribution to the scattering pattern of wind turbines in the uhf band. In *Antennas and Propagation (EUCAP), Proceedings of the 5th European Conference on*, pages 707–711. IEEE, 2011.

[10] Oleg A Krasnov and Alexander G Yarovoy. Radar micro-doppler of wind turbines: simulation and analysis using rotating linear wire structures. *International Journal of Microwave and Wireless Technologies*, 7(3-4):459–467, 2015.

[11] Faruk Uysal, Unnikrishna Pillai, Ivan Selesnick, and Braham Himed. Signal decomposition for wind turbine clutter mitigation. In *Radar Conference, 2014 IEEE*, pages 0060–0063. IEEE, 2014.

[12] Jakob J van Zyl. *Synthetic aperture radar polarimetry*, volume 2. John Wiley & Sons, 2011.

[13] Huub Nagel and Loek Colussi. Determination of the reflecting surface of a wind turbine, 2016.

[14] Stefano Medagli, Oleg A Krasnov, and Alexander G Yarovoy. Range segmentation for micro-doppler of backscattered field by wind turbines. In *Antennas and Propagation (EUCAP), 2017 11th European Conference on*, pages 263–267. IEEE, 2017.

[15] MA Richards, JA Scheer, and WA Holm. Principles of modern radar. vol. 1. *I: Basic Principles*, 2010.

[16] R Van der Heiden, LJ Van Ewijk, and FCA Groen. In-flight measurements and rcs-predictions: a comparison on broad-side radar range profiles of a boeing 737. 1997.

[17] Xuejun Liao and Zheng Bao. Radar target recognition using superresolution range profiles as features. In *International Symposium on Multispectral Image Processing (ISMIP'98)*, volume 3545, pages 397–401. International Society for Optics and Photonics, 1998.

[18] Rui Zhang, Xi Zhang Wei, and Xiang Li. The resolution of high resolution range profile for two ideal point targets. In *Information Science and Technology (ICIST), 2012 International Conference on*, pages 397–400. IEEE, 2012.

[19] Nadav Levanon. Stepped-frequency pulse-train radar signal. *IEE Proceedings-Radar, Sonar and Navigation*, 149(6):297–309, 2002.

[20] Thomas Perrott Gill. *The Doppler effect: an introduction to the theory of the effect*. Academic Press, 1965.

[21] Lawrence R Rabiner, Ronald W Schafer, et al. Introduction to digital speech processing. *Foundations and Trends® in Signal Processing*, 1(1–2):1–194, 2007.

[22] Florian Krug and Bastian Lewke. Electromagnetic interference on large wind turbines. *Energies*, 2(4):1118–1129, 2009.

[23] Kamal Sarabandi, Fawwaz T Ulaby, and M Ali Tassoudji. Calibration of polarimetric radar systems with good polarization isolation. *IEEE Transactions on Geoscience and Remote Sensing*, 28(1):70–75, 1990.

[24] Federal Meteorological Handbook. Doppler radar meteorological observations. part c, wsr-88d products and algorithms. Technical report, Technical Report, FCM-H11C-1991, Office of the Federal Coordinator for Meteorological Services and Supporting Research, Rockville, Maryland, 1991.

[25] Thomas Senior, Dipak L Sengupta, and Joseph E Ferris. Tv and fm interference by windmills. 1977.

[26] R Ryan Ohs, Gregory J Skidmore, and Gary Bedrosian. Modeling the effects of wind turbines on radar returns. In *military communications conference, 2010-milcom 2010*, pages 272–276. IEEE, 2010.

[27] HS Dabis and RJ Chignell. Wind turbine electromagnetic scatter modelling using physical optics techniques. *Renewable Energy*, 16(1-4):882–887, 1999.

[28] PJ Van Kats and OPE Pager. Reflections of electromagnetic waves by large wind turbines and their impact on uhf broadcast reception. *Report 511 TM/84, British Library*, 1984.

[29] David A Spera and Dipak L Sengupta. Equations for estimating the strength of tv signals scattered by wind turbines. 1994.

[30] JL Eaton, RI Black, and GH Taylor. Interference to television reception from large wind turbines. *NASA STI/Recon Technical Report N*, 83, 1983.

[31] Itziar Angulo, David de la Vega, Carlos Fernández, David Guerra, Yiyan Wu, Pablo Angueira, and Juan Luis Ordiales. An empirical comparative study of prediction methods for estimating multipath due to signal scattering from wind turbines on digital tv services. *IEEE Transactions on Broadcasting*, 57(2):195–203, 2011.

[32] Francesco Fioranelli, Matthew Ritchie, Alessio Balleri, and Hugh Griffiths. Practical investigation of multiband mono-and bistatic radar signatures of wind turbines. *IET Radar, Sonar & Navigation*, 2017.

[33] Fanxing Kong, Y Zhang, and Robert D Palmer. Wind turbine radar interference studies by polarimetric measurements of a scaled model. *IEEE Transactions on Aerospace and Electronic Systems*, 49(3):1589–1600, 2013.

[34] Gerhard Greving, Wolf-Dieter Biermann, and Rolf Mundt. Wind turbines as distorting scattering objects for radar-clutter aspects and visibility. In *Radar Symposium (IRS), 2010 11th International*, pages 1–4. IEEE, 2010.

[35] Aale Naqvi and Hao Ling. A study of radar features of wind turbines in the hf band. *Progress In Electromagnetics Research*, 143:605–621, 2013.

[36] Peter J Schubel and Richard J Crossley. Wind turbine blade design. *Energies*, 5(9):3425–3449, 2012.

[37] Y-X Liu, Xiang Li, and Z-W Zhuang. Estimation of micro-motion parameters based on micro-doppler. *IET signal processing*, 4(3):213–217, 2010.

[38] Andrew Lewis Maffett. *Topics for a statistical description of radar cross section*. Wiley New York, 1989.

[39] David C Jenn. Radar and laser cross section engineering(book). *Washington, DC: American Institute of Aeronautics and Astronautics, Inc, 1995.*, 1995.

[40] Brian M Kent, Kueichien C Hil, Alan Buterbaugh, Greg Zelinski, Robert Hawley, Lisa Cravens, Christopher Vogel, Thomas Coveyou, et al. Dynamic radar cross section and radar doppler measurements of commercial general electric windmill power turbines part 1: Predicted and measured radar signatures. *IEEE Antennas and Propagation Magazine*, 50(2):211–219, 2008.

[41] John T Moore, Arthur D Yaghjian, and Robert A Shore. Shadow boundary and truncated wedge ildcs in xpatch [radar applications]. In *Antennas and Propagation Society International Symposium, 2005 IEEE*, volume 1, pages 10–13. IEEE, 2005.

[42] I Angulo, D de la Vega, et al. Experimental results on wind turbines impact to terrestrial dtv reception in the uhf band. In *59th Annu. Broadcast Symp.(IEEE Broadcast Technol. Soc.)*, 2009.

[43] David De la Vega, C Fernandez, O Grande, I Angulo, D Guerra, Y Wu, P Angueira, and JL Ordiales. Software tool for the analysis of potential impact of wind farms on radiocommunication services. In *Broadband Multimedia Systems and Broadcasting (BMSB), 2011 IEEE International Symposium on*, pages 1–5. IEEE, 2011.

[44] E Miller, G Pjerrou, and E Selden. On the versatility of thin-wire electric field integral equation techniques. In *Antennas and Propagation Society International Symposium, 1969*, volume 7, pages 17–25. IEEE, 1969.

[45] J Pinto, JCG Matthews, and C Sarno. Radar signature reduction of wind turbines through the application of stealth technology. In *Antennas and Propagation, 2009. EuCAP 2009. 3rd European Conference on*, pages 3886–3890. IEEE, 2009.

[46] LS Rashid and AK Brown. Radar cross-section analysis of wind turbine blades with radar absorbing materials. In *Radar Conference (EuRAD), 2011 European*, pages 97–100. IEEE, 2011.

[47] A Tennant and B Chambers. Signature management of radar returns from wind turbine generators. *Smart materials and structures*, 15(2):468, 2006.

[48] Laith S Rashid and Anthony K Brown. Rcs and radar propagation near offshore wind farms. In *Antennas and Propagation Society International Symposium, 2007 IEEE*, pages 4605–4608. IEEE, 2007.

[49] B Lewke, F Krug, and J Kindersberger. Mom based emi analysis on large wind turbine gsm 900 mhz communication backup-system. In *Electromagnetic Compatibility, 2007. EMC Zurich 2007. 18th International Zurich Symposium on*, pages 183–186. IEEE, 2007.

[50] A Balanis Constantine et al. Antenna theory: analysis and design. *MICROSTRIP ANTENNAS, third edition, John wiley & sons*, 2005.

[51] Nicholas J Willis. *Bistatic radar*, volume 2. SciTech Publishing, 2005.